Virtual crack closure technique: History, approach, and applications

Ronald Krueger

National Institute of Aerospace, Hampton, Virginia 23666
rkrueger@nianet.org

An overview of the virtual crack closure technique is presented. The approach used is discussed, the history summarized, and insight into its applications provided. Equations for two-dimensional quadrilateral finite elements with linear and quadratic shape functions are given. Formulas for applying the technique in conjunction with three-dimensional solid elements as well as plate/shell elements are also provided. Necessary modifications for the use of the method with geometrically nonlinear finite element analysis and corrections required for elements at the crack tip with different lengths and widths are discussed. The problems associated with cracks or delaminations propagating between different materials are mentioned briefly, as well as a strategy to minimize these problems. Due to an increased interest in using a fracture mechanics–based approach to assess the damage tolerance of composite structures in the design phase and during certification, the engineering problems selected as examples and given as references focus on the application of the technique to components made of composite materials. [DOI: 10.1115/1.1595677]

Keywords: Finite Element Analysis, Fracture Mechanics, Crack Closure Integral, Composite Structures, Delamination, Interlaminar Fracture

1 INTRODUCTION

One of the most common failure modes for composite structures is delamination [1–4]. The remote loadings applied to composite components are typically resolved into interlaminar tension and shear stresses at discontinuities that create mixed-mode I, II, and III delaminations. To characterize the onset and growth of these delaminations the use of fracture mechanics has become common practice over the past two decades [5–7]. The total strain energy release rate, G_T, the mode I component due to interlaminar tension, G_I, the mode II component due to interlaminar sliding shear, G_{II}, and the mode III component, G_{III}, due to interlaminar scissoring shear, as shown in Fig. 1, need to be calculated. In order to predict delamination onset or growth for two-dimensional problems, these calculated G components are compared to interlaminar fracture toughness properties measured over a range from pure mode I loading to pure mode II loading [8–13]. A quasistatic mixed-mode fracture criterion is determined by plotting the interlaminar fracture toughness, G_c, versus the mixed-mode ratio, G_I/G_T, determined from data generated using pure mode I Double Cantilever Beam (DCB) ($G_{II}/G_T=0$), pure mode II End Notched Flexure (4ENF) ($G_{II}/G_T=1$), and mixed-mode Mixed Mode Bending (MMB) tests of varying ratios, as shown in Fig. 2 for IM7/8552 [14]. A curve fit of these data is performed to determine

a mathematical relationship between G_c and G_{II}/G_T [6]. Failure is expected when, for a given mixed-mode ratio G_{II}/G_T, the calculated total energy release rate, G_T, exceeds the interlaminar fracture toughness, G_c. Although several specimens have also been suggested for the measurement of the mode III interlaminar fracture toughness property [15–18], an interaction criterion incorporating the scissoring shear has not yet been established. The virtual crack closure technique (VCCT) [19–23] is widely used for computing energy release rates based on results from continuum (2D) and solid (3D) finite element (FE) analyses to supply the mode separation required when using the mixed-mode fracture criterion.

Although the original publication on VCCT dates back a quarter century [19], the virtual crack closure technique has not yet been implemented into any of the large commercial general purpose finite element codes such as MSC NASTRAN, ABAQUS, ANSYS, ASKA, PERMAS or SAMCEF. Currently FRANC2D, developed by the Cornell Fracture Group (CFG) at Cornell University, appears to be the only publically available, highly specialized finite element code that uses the virtual crack closure technique [24,25]. The virtual crack closure technique has been used mainly by scientists in universities, research institutions, and government laboratories and is usually implemented in their own specialized codes or used in postprocessing routines in conjunction with

general purpose finite element codes. Lately, an increased interest in using a fracture mechanics–based approach to assess the damage tolerance of composite structures in the design phase and during certification has also renewed the interest in the virtual crack closure technique [4,23]. Efforts are underway to incorporate these approaches in the *Composites Material MIL-17 Handbook*.[1]

The goal of the current paper is to give an overview of the virtual crack closure technique, discuss the approach used, summarize the history, and provide insight into its application. Equations for two-dimensional quadrilateral elements with linear and quadratic shape functions will be provided. Formulas for applying the technique in conjunction with three-dimensional solid elements as well as plate/shell elements will also be given. Necessary modifications for the use of the method with geometrically nonlinear finite element analysis and corrections required for elements at the crack tip with different lengths and widths will be discussed. The problems associated with cracks or delaminations propagating between different materials (the so-called bimaterial interface) will be mentioned briefly, as well as a strategy to minimize these problems. The selected engineering problems shown as examples and given as references will focus on the application of the technique related to composite materials as mentioned above.

2 BACKGROUND

A variety of methods are used to compute the strain energy release rate based on results obtained from finite element analysis. The *finite crack extension method* [26,27] requires two complete analyses. In the model the crack gets extended for a finite length prior to the second analysis. The method provides one global total energy release rate as global forces on a structural level are multiplied with global deformations to calculate the energy available to advance the crack. The *virtual crack extension method* [28–37] requires only one complete analysis of the structure to obtain the deformations. The total energy release rate or *J integral* is computed locally at the crack front and the calculation only involves an additional computation of the stiffness matrix of the elements affected by the virtual crack extension. The method yields the total energy release rate as a function of the direction in

which the crack was extended virtually, yielding information on the most likely growth direction. Modifications of the method have been suggested in the literature to allow the mode separation for two-dimensional analysis [38,39]. An *equivalent domain integral method* that can be applied to both linear and nonlinear problems and additionally allows for mode separation was proposed in Refs. [40–45]. The methods above have been mentioned here briefly to complement the background information. A comprehensive overview of different methods used to compute energy release rates is given in Ref. [46]. Alternative approaches to compute the strain energy release rate based on results obtained from finite element analysis have also been published recently [47–49].

For delaminations in laminated composite materials where the failure criterion is highly dependent on the mixed-mode ratio and propagation occurs in the laminate plane, the virtual crack closure technique [19–22] has been most widely used for computing energy release rates because fracture mode separation is determined explicitly. Recently new VCCT methods to compute mixed-mode energy release rates suitable for the application with the *p* version of the finite element method have also been developed [50]. Some modified and newly developed formulations of the VCCT allow applications that are not based on finite element analysis and are suitable for boundary element analysis [25,51].

2.1 Crack closure method using two analysis steps

Even though the virtual crack closure technique is the focus of this paper and is generally mentioned in the literature, it appears appropriate to include a related method: the *crack closure method* or *two-step crack closure technique*. The terminology in the literature is often inexact and this two-step method is sometimes referred to as VCCT. It may be more appropriate to call the method the *crack closure method* because the crack is physically extended, or closed, during two complete finite element analyses as shown in Fig. 3. The crack closure method is based on Irwin's crack closure integral [52,53]. The method is based on the assumption that the energy ΔE released when the crack is extended by Δa from a [Fig. 3(a)] to $a + \Delta a$ [Fig. 3(b)] is identical to the energy

---

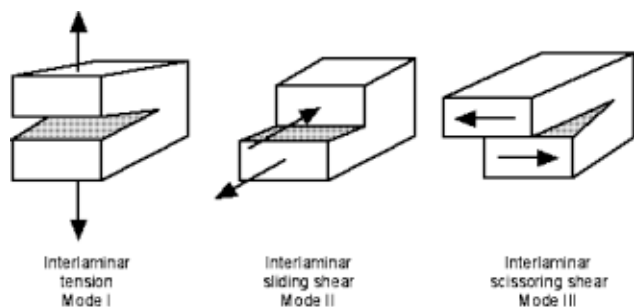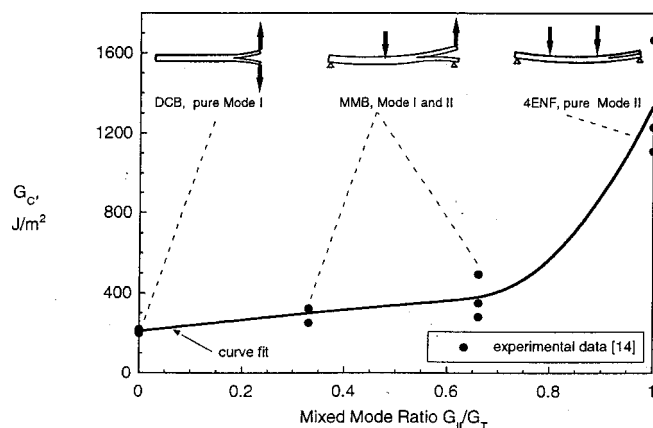[1]http://www.mil17.org/

Fig. 1   Fracture modes

Fig. 2   Mixed-mode delamination criterion for IM7/8552

required to close the crack between location ℓ and i [Fig. 3(a)]. Index 1 denotes the first step depicted in Fig. 3(a) and index 2 the second step as shown in Fig. 3(b). For a crack modeled with two-dimensional four-noded elements as shown in Fig. 3 the work ΔE required to close the crack along one element side can be calculated as

$$\Delta E = \tfrac{1}{2}[X_{1\ell}\Delta u_{2\ell} + Z_{1\ell}\Delta w_{2\ell}], \tag{1}$$

where $X_{1\ell}$ and $Z_{1\ell}$ are the shear and opening forces at nodal point ℓ to be closed [Fig. 3(a)] and $\Delta u_{2\ell}$ and $\Delta w_{2\ell}$ are the differences in shear and opening nodal displacements at node ℓ as shown in Fig. 3(b). The crack closure method establishes the original condition before the crack was extended. Therefore the forces required to close the crack are identical to the forces acting on the upper and lower surfaces of the closed crack. The forces $X_{1\ell}$ and $Z_{1\ell}$ may be obtained from a first finite element analysis where the crack is closed as shown in Fig. 3(a) by summing the forces at common nodes from elements belonging either to the upper or the lower surface. Forces at constraints may also be used if this option is available in the finite element software used. The options are discussed in detail in the Appendix. The displacements $\Delta u_{2\ell}$ and $\Delta w_{2\ell}$ are obtained from a second finite element analysis where the crack has been extended to its full length $a + \Delta a$ as shown in Fig. 3(b).

2.2 The modified crack closure method

The modified, or virtual, crack closure method (VCCT) is based on the same assumptions as the crack closure method described above. Additionally, however, it is assumed that a crack extension of Δa from $a + \Delta a$ (node i) to $a + 2\Delta a$ (node k) does not significantly alter the state at the crack tip (Fig. 4). Therefore, when the crack tip is located at node k, the displacements behind the crack tip at node i are approximately equal to the displacements behind the crack tip at node ℓ when the crack tip is located at node i. Further, the energy ΔE released when the crack is extended by Δa from $a + \Delta a$ to $a + 2\Delta a$ is identical to the energy required to close the crack between location i and k. For a crack modeled with

where $Z_{1\ell}^{l} = Z_{1\ell}^{u}$ and $X_{1\ell}^{l} = X_{1\ell}^{u}$ from equilibrium
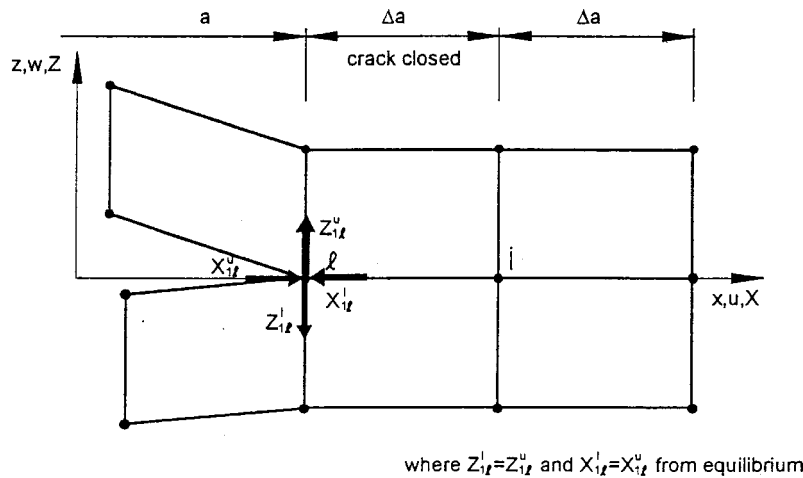
(a). *First Step - Crack closed*
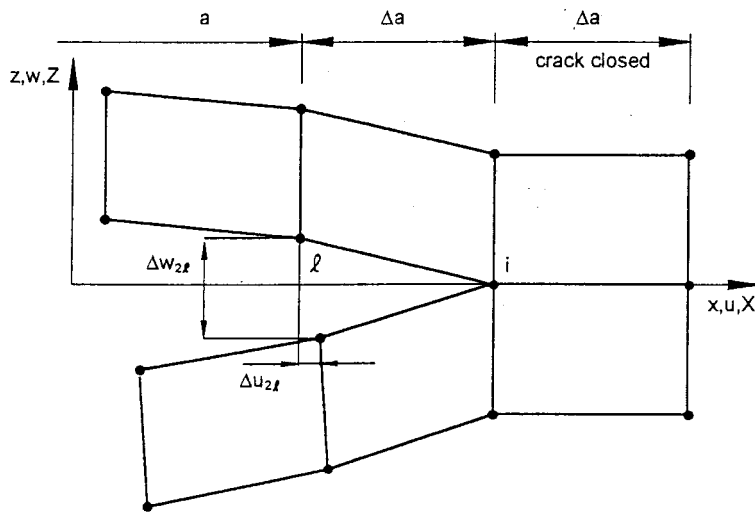
(b). *Second Step - Crack extended*

Fig. 3   Crack closure method (two-step method). a) First step—crack closed and b) second step—crack extended.

two-dimensional, four-noded elements, as shown in Fig. 4, the work ΔE required to close the crack along one element side therefore can be calculated as

$$\Delta E = \tfrac{1}{2}[X_i \Delta u_\ell + Z_i \Delta w_\ell], \tag{2}$$

where X_i and Z_i are the shear and opening forces at nodal point i and Δu_ℓ and Δw_ℓ are the shear and opening displacements at node ℓ as shown in Fig. 4. Thus, forces and displacements required to calculate the energy ΔE to close the crack may be obtained from one single finite element analysis. The details of calculating the energy release rate $G = \Delta E / \Delta A$, where ΔA is the crack surface created, and the separation into the individual mode components will be discussed in the following section.

3   EQUATIONS FOR USING THE VIRTUAL CRACK CLOSURE TECHNIQUE

In the following, equations are presented to calculate mixed-mode strain energy release rates using two-dimensional finite element models such as plane stress or plane strain. Different approaches are also discussed for the cases where the crack or delamination is modeled with plate/shell elements or with three-dimensional solids.

3.1   Formulas for two-dimensional analysis

In a two-dimensional finite element plane stress, or plane strain model, the crack of length a is represented as a one-dimensional discontinuity by a line of nodes as shown in Fig. 5. Nodes at the top surface and the bottom surface of the discontinuity have identical coordinates, however, and are not connected with each other as shown in Fig. 5(a). This lets the elements connected to the top surface of the crack deform independently from those connected to the bottom surface and allows the crack to open as shown in Fig. 5(b). The crack tip and the undamaged section, or the section where the crack is closed and the structure is still intact, is
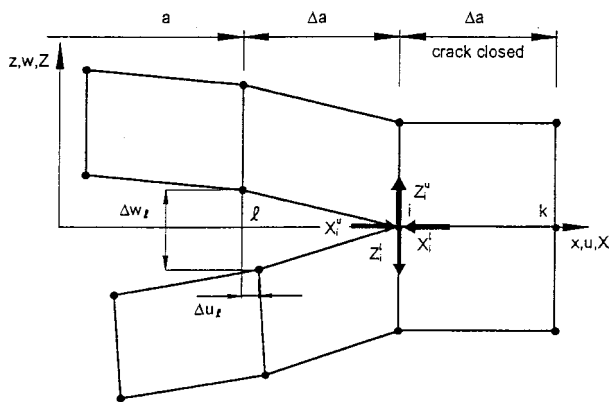
modeled using single nodes, or two nodes with identical coordinates coupled through multipoint constraints if a crack propagation analysis is desired. This is discussed in detail in the Appendix, which explains specific modeling issues.

For a crack propagation analysis, it is important to advance the crack in a kinematically compatible way. Nodewise opening/closing, where node after node is sequentially released along the crack, is possible for the four-noded element as shown in Fig. 6(a). It is identical to elementwise opening in this case as the crack is opened over the entire length of the element. Nodewise opening/closing, however, results in kinematically incompatible interpenetration for the eight-noded elements with quadratic shape functions as shown in Fig. 6(b), which caused initial problems when eight-noded elements were used in connection with the virtual crack closure technique. Elementwise opening—where edge and midside nodes are released—provides a kinematically compatible condition and yields reliable results, which was demonstrated in Refs. [5],[54],[55] and later generalized expressions to achieve this were derived by Raju [21].

The mode I and mode II components of the strain energy release rate, G_I and G_{II}, are calculated for four-noded elements as shown in Fig. 7(a):
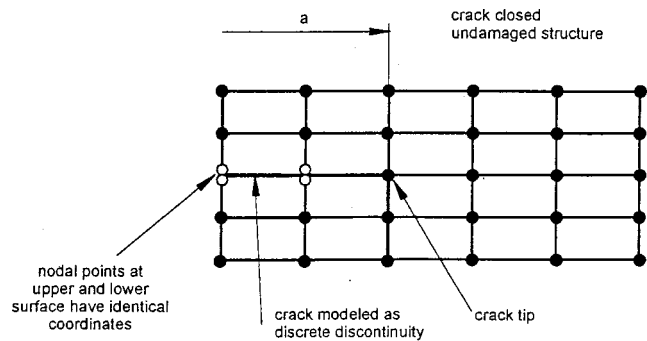
$$G_I = -\frac{1}{2\Delta a} Z_i (w_\ell - w_{\ell*}), \tag{3}$$

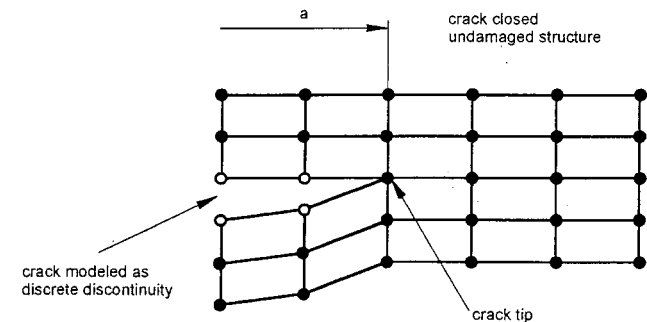$$G_{II} = -\frac{1}{2\Delta a} X_i (u_\ell - u_{\ell*}), \tag{4}$$

(a). *Initially modeled, undeformed finite element mesh*

(b). *Deformed finite element mesh*

Fig. 5   Crack modeled as one-dimensional discontinuity. *a)* Initially modeled, undeformed finite element mesh and *b)* deformed finite element mesh.
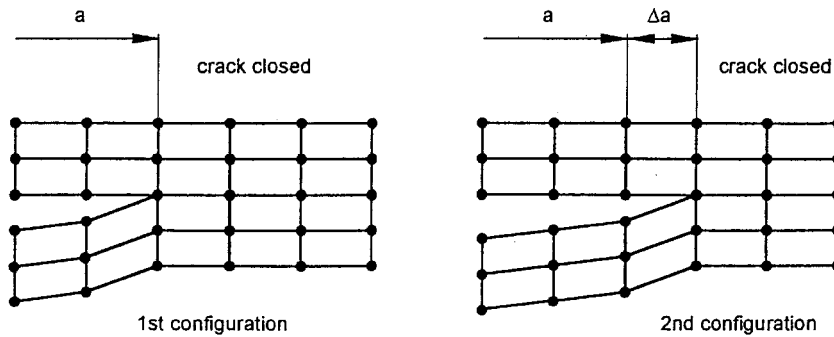

Fig. 4   Modified crack closure method (one-step VCCT)

where Δa is the length of the elements at the crack front and X_i and Z_i are the forces at the crack tip (nodal point i). The relative displacements behind the crack tip are calculated from the nodal displacements at the upper crack face u_ℓ and w_ℓ (nodal point ℓ) and the nodal displacements $u_{\ell*}$ and $w_{\ell*}$ at the lower crack face (nodal point ℓ^*), respectively. The crack surface ΔA created is calculated as $\Delta A = \Delta a \times 1$, where it is assumed that the two-dimensional model is of unit thickness 1. While the original paper by Rybicki and Kanninen is based on heurisitic arguments [19], Raju proved the validity of the equation [21]. He also showed that the equations are applicable if triangular elements, obtained by collapsing the rectangular elements, are used at the crack tip.

The mode I and mode II components of the strain energy release rate, G_I, and G_{II}, are calculated for eight-noded elements as shown in Fig. 7(b):

$$G_I = -\frac{1}{2\Delta a}[Z_i(w_\ell - w_{\ell*}) + Z_j(w_m - w_{m*})], \tag{5}$$

$$G_{II} = -\frac{1}{2\Delta a}[X_i(u_\ell - u_{\ell*}) + X_j(u_m - u_{m*})], \tag{6}$$

where Δa is the length of the elements at the crack front as above. In addition to the forces X_i and Z_i at the crack tip (nodal point i) the forces X_j and Z_j at the midside node in front of the crack (nodal point j) are required. The relative sliding and opening behind the crack tip are calculated at nodal points ℓ and ℓ^* from displacements at the upper crack face u_ℓ and w_ℓ and the displacements $u_{\ell*}$ and $w_{\ell*}$ at the lower crack face. In addition to the relative displacements at nodal points ℓ and ℓ^* the relative displacements at nodal points m and m^* are required, which are calculated from
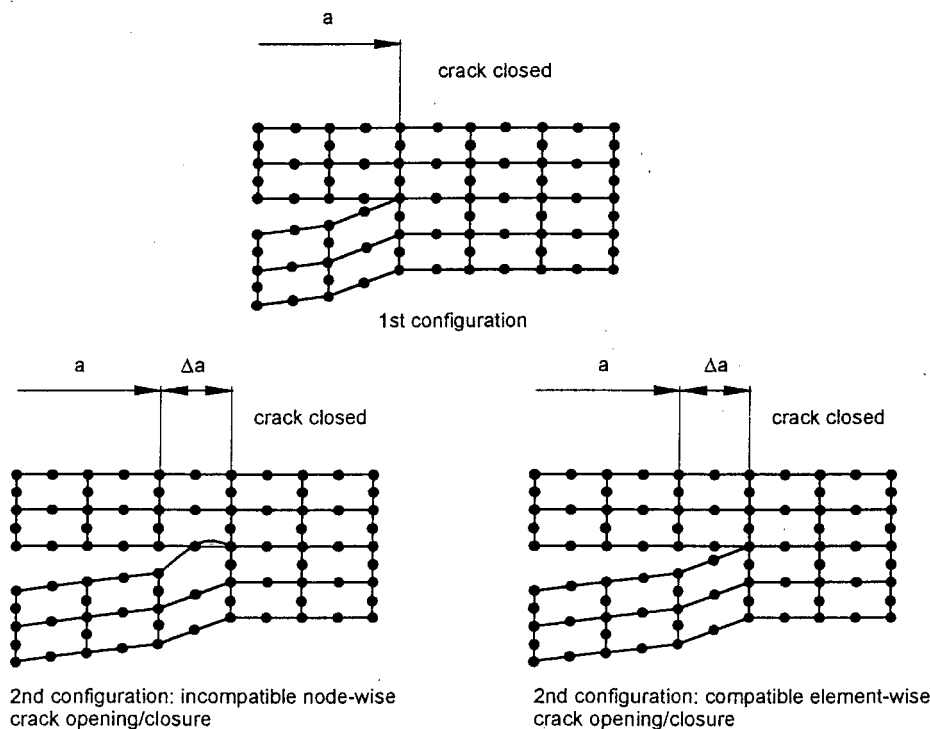
(a). *Node wise crack opening for four-noded element*

Fig. 6 Kinematic compatible crack opening/closure. *a*) Node-wise crack opening for four-noded element and *b*) crack opening for eight-noded element.

(b). *Crack opening for eight-noded element*

displacements at the upper crack face u_m and w_m and the displacements u_{m*} and w_{m*} at the lower crack face [21]. The crack surface ΔA created is calculated as $\Delta A = \Delta a \times 1$, where it is assumed that the two-dimensional model is of unit thickness 1. The equations are also applicable if triangular parabolic elements, obtained by collapsing the parabolic rectangular elements, are used at the crack tip [21]. The total energy release rate G_T is calculated from the individual mode components as

$$G_T = G_I + G_{II} + G_{III}, \tag{7}$$

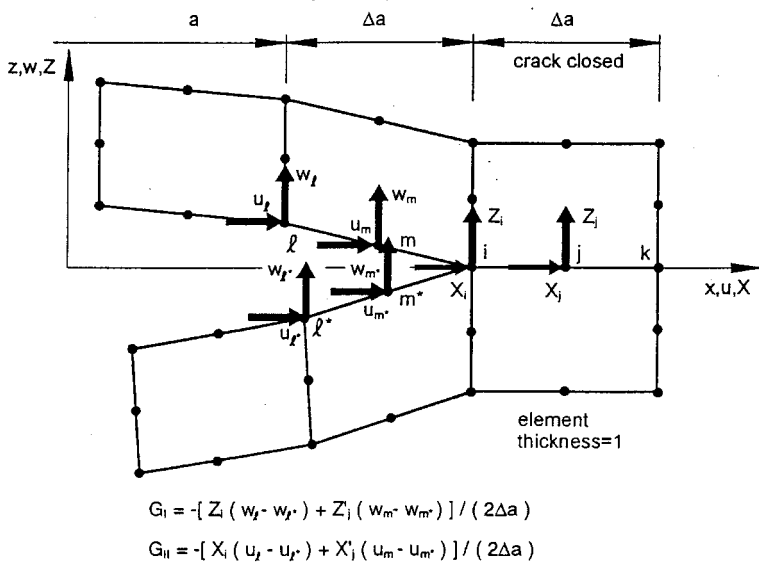where $G_{III} = 0$ for the two-dimensional case discussed.

The VCCT proposed by Rybicki and Kanninen did not make any assumptions of the form of the stresses and displacements. Therefore, singularity elements are not required

at the crack tip. However, special two-dimensional crack tip elements with quarter-point nodes as shown in Fig. 8 have been proposed in the literature [21,56–58]. Based on the location of the nodal points at $\xi = 0.0$, 0.25, and 1.0, these quarter-point elements accurately simulate *the* $1/\sqrt{r}$ singularity of the stress field at the crack tip. Triangular quarter-point elements are obtained by collapsing one side of the rectangular elements, as shown in Fig. 8(b). The mode I and mode II components of the strain energy release rate, G_I, and G_{II} are calculated for eight-noded singularity elements using the simplified equations given in Ref. [21]:

$$G_I = -\frac{1}{2\Delta a}[Z_i\{t_{11}(w_\ell - w_{\ell*}) + t_{12}(w_m - w_{m*})\} + Z_j\{t_{21}(w_\ell - w_{\ell*}) + t_{22}(w_m - w_{m*})\}], \tag{8}$$
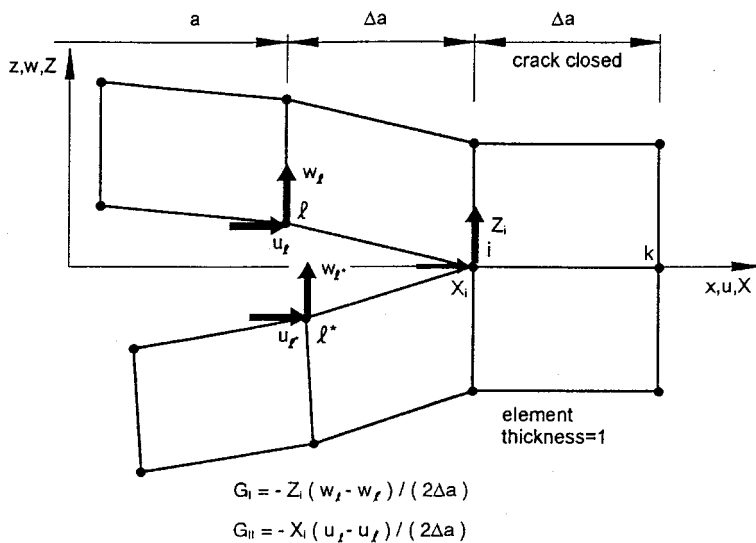
$$G_I = - Z_i (w_\ell - w_{\ell^*}) / (2\Delta a)$$

$$G_{II} = - X_i (u_\ell - u_{\ell^*}) / (2\Delta a)$$

(a). *Virtual Crack Closure Technique for four-noded element (lower surface forces are omitted for clarity).*

$$G_I = -[Z_i (w_\ell - w_{\ell^*}) + Z'_j (w_m - w_{m^*})] / (2\Delta a)$$

$$G_{II} = -[X_i (u_\ell - u_{\ell^*}) + X'_j (u_m - u_{m^*})] / (2\Delta a)$$

(b). *Virtual Crack Closure Technique for eight-noded element (lower surface forces are omitted for clarity).*

Fig. 7   Virtual crack closure technique for 2D solid elements. *a*) Virtual crack closure technique for four-noded element (lower surface forces are omitted for clarity) and *b*) virtual crack closure technique for eight-noded element (lower surface forces are omitted for clarity).

$$G_{\mathrm{II}} = -\frac{1}{2\Delta a}[X_i\{t_{11}(u_\ell - u_{\ell*}) + t_{12}(u_m - u_{m*})\}$$

$$+ X_j\{t_{21}(u_\ell - u_{\ell*}) + t_{22}(u_m - u_{m*})\}], \tag{9}$$

where

$$t_{11} = 6 - \frac{3\pi}{2}, \quad t_{12} = 6\pi - 20, \quad t_{21} = \frac{1}{2}, \quad t_{22} = 1. \tag{10}$$

In contrast to regular parabolic elements, Eqs. (8) and (9) for the quarter-point elements have cross terms involving the

corner and quarter-point forces and the relative displacements at the corner and quarter-point nodes. Equations (8) and (9) are also valid if triangular quarter-point elements, obtained by collapsing one side of the rectangular elements, are used at the crack tip as shown in Fig. 8(b). Note that for triangular elements the nodal forces have to be calculated from elements A, B, C, and D around the crack tip. Special rectangular and collapsed singularity elements with cubic shape functions are also discussed in Ref. [21]. A special six-noded rectangular element with quarter-point nodes is described in Ref. [59]. Due to the fact that these elements are not readily available in most of the commonly used finite

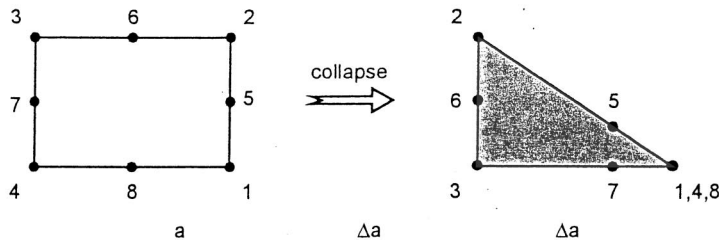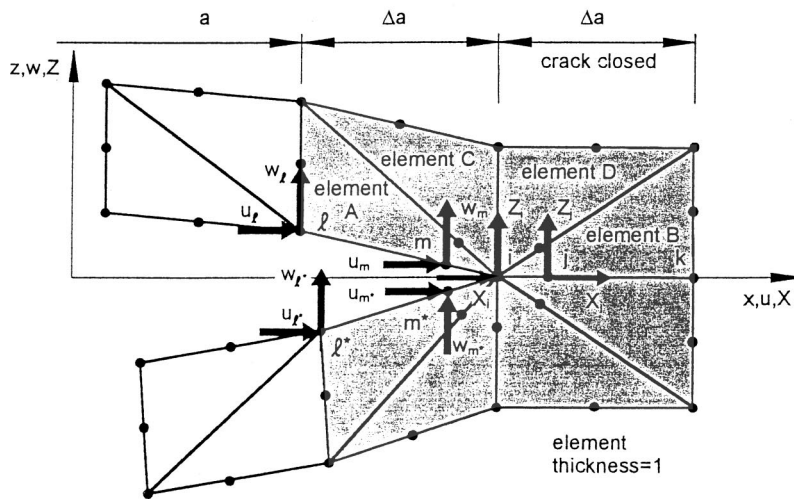(a). *Quadtrilateral elements with quarter point nodes.*
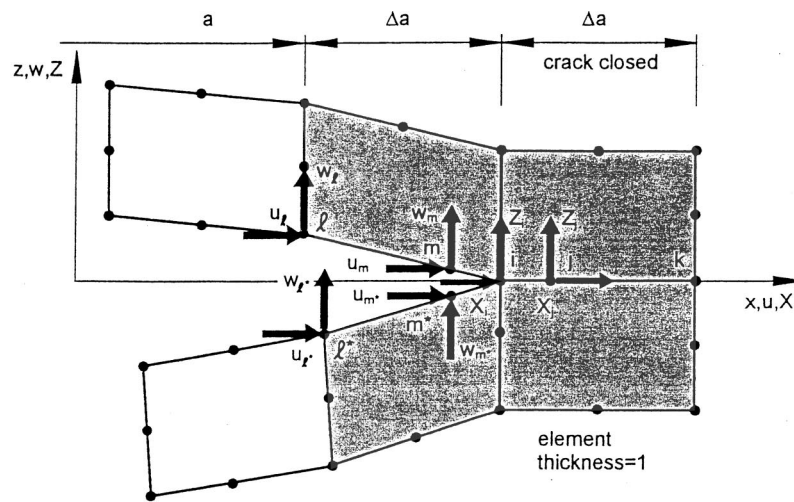
(b). *Collapsed quarter point element.*

Fig. 8 Singularity elements with quarter-point nodes at crack tip. *a*) Quadrilateral elements with quarter-point nodes and *b*) collapsed quarter-point element.

element codes, equations are not provided. For additional information about singularity elements the interested reader is referred to Refs. [58],[60–64].

3.2 Formulas for three-dimensional solids and plate/ shell elements

In a finite element model made of three-dimensional solid elements [Fig. 9(*a*)] or plate or shell type elements [Fig. 9(*b*)] the delamination of length *a* is represented as a two-dimensional discontinuity by two surfaces. The additional dimension allows us to calculate the distribution of the energy release rates along the delamination front and makes it possible to obtain G_{III}, which is identical to zero for two-dimensional models. Nodes at the top surface and the bottom

surface have identical coordinates and are not connected with each other as explained in the preceding section. The delamination front is represented by either a row of single nodes or two rows of nodes with identical coordinates, coupled through multipoint constraints. The undamaged section where the delamination is closed and the structure is intact is modeled using single nodes or two nodes with identical coordinates coupled through multipoint constraints if a delamination propagation analysis is desired. This is discussed in detail in the Appendix, which explains specific modeling issues.
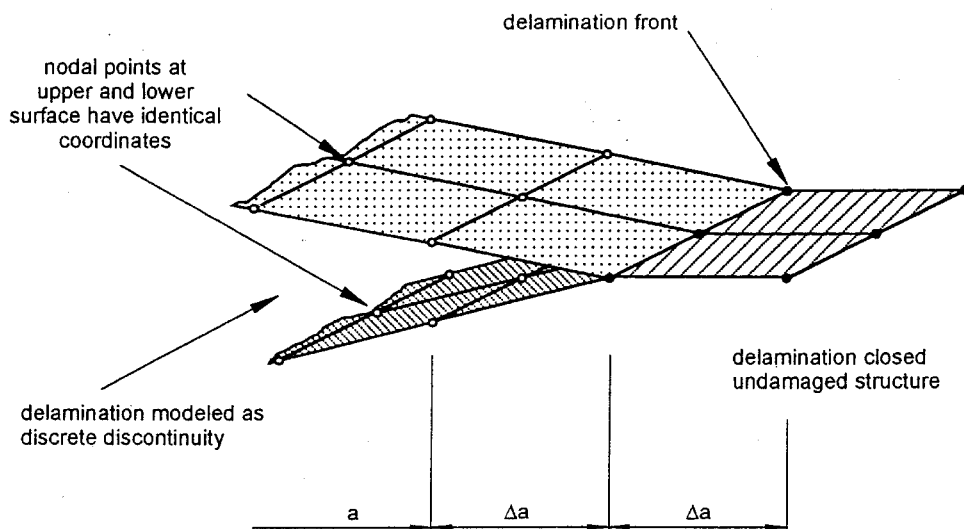
3.2.1 Formulas for three-dimensional solids
For convenience, only a section of the delaminated area that is modeled with eight-noded three-dimensional solid ele-
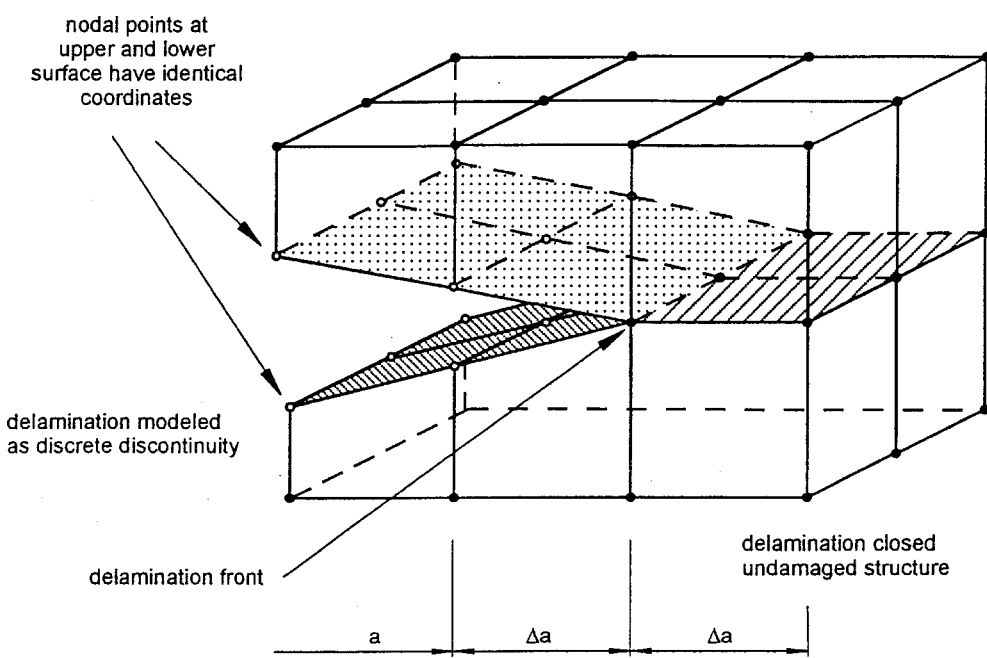
(a). *Delamination modeled with bilinear three-dimensional solid elements*

(b). *Delamination modeled with bilinear plate/shell type elements*

Fig. 9 Delaminations modeled as two-dimensional discontinuity. *a*) Delamination modeled with bilinear 3D solid elements and *b*) delamination modeled with bilinear plate/shell type elements.

ments is illustrated in Fig. 10. The mode I, mode II, and mode III components of the strain energy release rate, G_I, G_II, and G_III, are calculated as

$$G_\mathrm{I} = -\frac{1}{2\Delta A} Z_{Li}(w_{L\ell} - w_{L\ell*}), \tag{11}$$

$$G_\mathrm{II} = -\frac{1}{2\Delta A} X_{Li}(u_{L\ell} - u_{L\ell*}), \tag{12}$$

$$G_\mathrm{III} = -\frac{1}{2\Delta A} Y_{Li}(v_{L\ell} - v_{L\ell*}), \tag{13}$$

with $\Delta A = \Delta a b$ as shown in Fig. 10 [65]. Here ΔA is the area virtually closed, Δa is the length of the elements at the delamination front, and b is the width of the elements. For

better identification in this and the following figures, columns are identified by capital letters and rows by small letters as illustrated in the top view of the upper surface shown in Fig. 10(b). Hence, X_{Li}, Y_{Li}, and Z_{Li} denote the forces at the delamination front in column L, row i. The corresponding displacements behind the delamination at the top face node row ℓ are denoted $u_{L\ell}$, $v_{L\ell}$, and $w_{L\ell}$ and at the lower face node row $\ell*$ are denoted $u_{L\ell*}$, $v_{L\ell*}$, and $w_{L\ell*}$ as shown in Fig. 10. All forces and displacements are obtained from the finite element analysis with respect to the global system. A local crack tip coordinate system (x', y', z') that defines the normal and tangential coordinate directions at the delamination front in the deformed configuration has been added to the illustration. Its use with respect to geometrically nonlinear analyses will be discussed later.

For twenty-noded solid elements, the equations to calculate the strain energy release rate components at the element corner nodes (location Li) as shown in Fig. 11 are

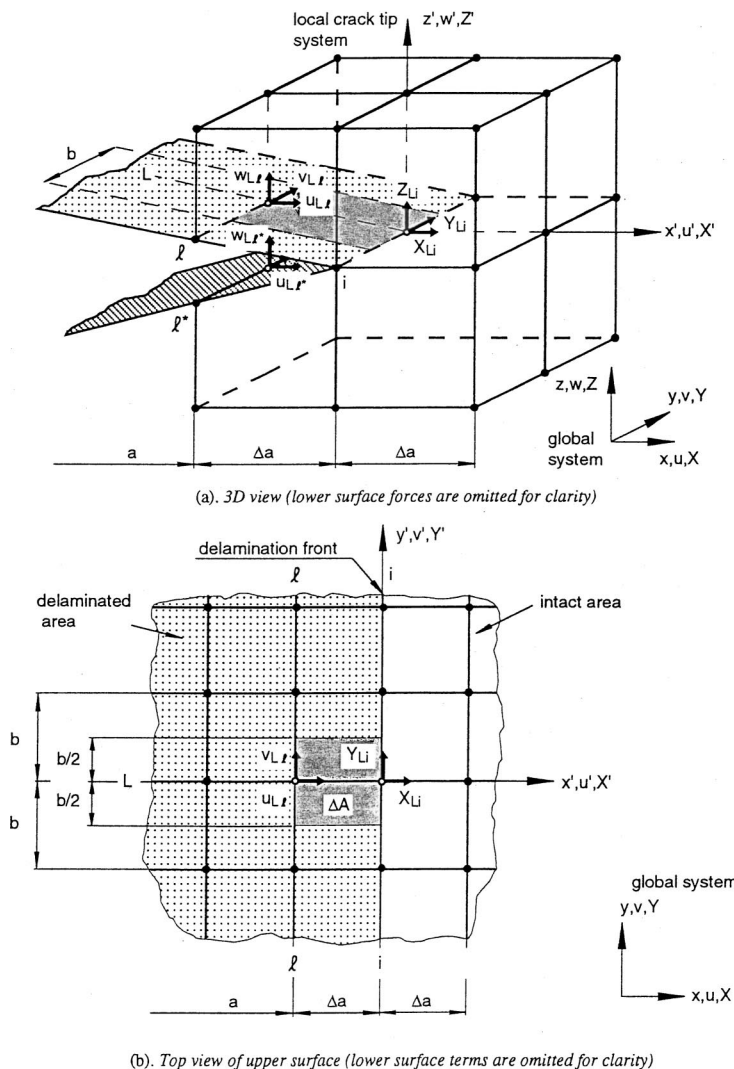(a). 3D view (lower surface forces are omitted for clarity)

Fig. 10   Virtual crack closure technique for four-noded plate/shell and eight-noded solid elements. a) 3D view (lower surface forces are omitted for clarity) and b) top view of upper surface (lower surface terms are omitted for clarity).

(b). Top view of upper surface (lower surface terms are omitted for clarity)

$$G_I = -\frac{1}{2\Delta A_L}\left[\tfrac{1}{2}Z_{Ki}(w_{K\ell}-w_{K\ell *})+Z_{Li}(w_{L\ell}-w_{L\ell *})\right.$$

$$\left.+Z_{Lj}(w_{Lm}-w_{Lm*})+\tfrac{1}{2}Z_{Mi}(w_{M\ell}-w_{M\ell *})\right], \qquad (14)$$

$$G_{II} = -\frac{1}{2\Delta A_L}\left[\tfrac{1}{2}X_{Ki}(u_{K\ell}-u_{K\ell *})+X_{Li}(u_{L\ell}-u_{L\ell *})\right.$$

$$\left.+X_{Lj}(u_{Lm}-u_{Lm*})+\tfrac{1}{2}X_{Mi}(u_{M\ell}-u_{M\ell *})\right], \qquad (15)$$

$$G_{III} = -\frac{1}{2\Delta A_L}\left[\tfrac{1}{2}Y_{Ki}(v_{K\ell}-v_{K\ell *})+Y_{Li}(v_{L\ell}-v_{L\ell *})\right.$$

$$\left.+Y_{Lj}(v_{Lm}-v_{Lm*})+\tfrac{1}{2}Y_{Mi}(v_{M\ell}-v_{M\ell *})\right], \qquad (16)$$

where $\Delta A_L = \Delta ab$ as shown in Fig. 11 [66]. Here X_{Ki}, Y_{Ki},

and Z_{Ki} denote the forces at the delamination front in column K, row i. The relative displacements at the corresponding column K are calculated from the displacements behind the delamination at the lower face node row ℓ^* as $u_{K\ell *}$, $v_{K\ell *}$, and $w_{K\ell *}$ and at the top face node row ℓ, as $u_{K\ell}$, $v_{K\ell}$ and $w_{K\ell}$ [Fig. 11(b)]. Similar definitions are applicable in column M for the forces at node row i and displacements at node row ℓ and in column L for the forces at node row i and j and displacements at node row ℓ and m, respectively. Only one half of the forces at locations Ki and Mi contribute to the energy required to virtually close the area ΔA_L. Half of the forces at location Ki contribute to the closure of the adjacent area ΔA_J and half of the forces at location Mi contribute to the closure of the adjacent area ΔA_N.

The equations to calculate the strain energy release rate components at the midside node (location Mi) as shown in Fig. 12 are as follows [66,67]:
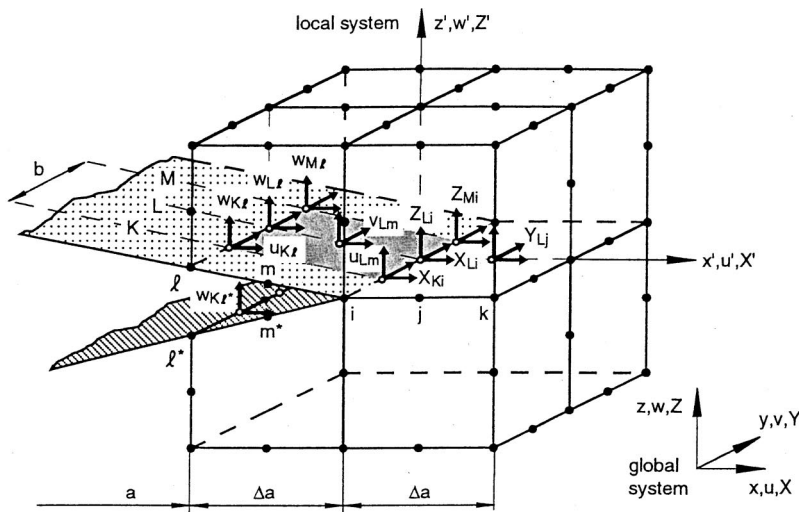
(a). 3D view (lower surface forces are omitted for clarity)
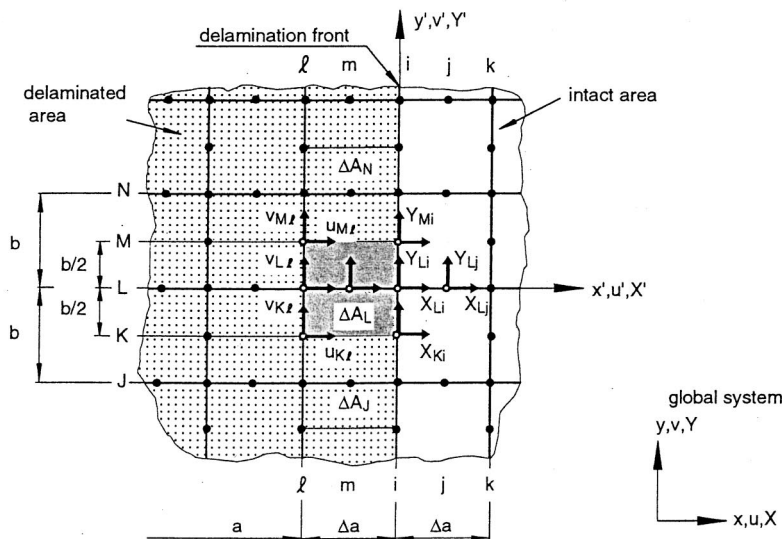
(b). Top view of upper surface (lower surface terms are omitted for clarity)

Fig. 11   Virtual crack closure technique for corner nodes in eight-noded plate/shell and twenty-noded solid-elements. a) 3D view (lower surface forces are omitted for clarity) and b) top view of upper surface (lower surface terms are omitted for clarity).

$$G_{\mathrm{I}} = -\frac{1}{2\Delta A_M}\left[\frac{1}{2}Z_{Li}(w_{L\ell}-w_{L\ell *})+\frac{1}{2}Z_{Lj}(w_{Lm}-w_{Lm *})\right.$$

$$+Z_{Mi}(w_{M\ell}-w_{M\ell *})+\frac{1}{2}Z_{Ni}(w_{N\ell}-w_{N\ell *})$$

$$\left.+\frac{1}{2}Z_{Nj}(w_{Nm}-w_{Nm *})\right], \tag{17}$$

$$G_{\mathrm{II}} = -\frac{1}{2\Delta A_M}\left[\frac{1}{2}X_{Li}(u_{L\ell}-u_{L\ell *})+\frac{1}{2}X_{Lj}(u_{Lm}-u_{Lm *})\right.$$

$$+X_{Mi}(u_{M\ell}-u_{M\ell *})+\frac{1}{2}X_{Ni}(u_{N\ell}-u_{N\ell *})$$

$$\left.+\frac{1}{2}X_{Nj}(u_{Nm}-u_{Nm *})\right], \tag{18}$$

$$G_{\mathrm{III}} = -\frac{1}{2\Delta A_M}\left[\frac{1}{2}Y_{Li}(v_{L\ell}-v_{L\ell *})+\frac{1}{2}Y_{Lj}(v_{Lm}-v_{Lm *})\right.$$

$$+Y_{Mi}(v_{M\ell}-v_{M\ell *})+\frac{1}{2}Y_{Ni}(v_{N\ell}-v_{N\ell *})$$

$$\left.+\frac{1}{2}Y_{Nj}(v_{Nm}-v_{Nm *})\right], \tag{19}$$

where only one half of the forces at locations Li, Lj and Ni, Nj contribute to the energy required to virtually close the area ΔA_M. Half of the forces at locations Li and Lj contribute to the closure of the adjacent area ΔA_K and half of the forces at locations Ni and Nj contribute to the closure of the adjacent area ΔA_0.

Instead of computing the strain energy release rate components at the corner or midside nodes as described above, G_{I}, G_{II}, and G_{III} may be calculated for an entire element,
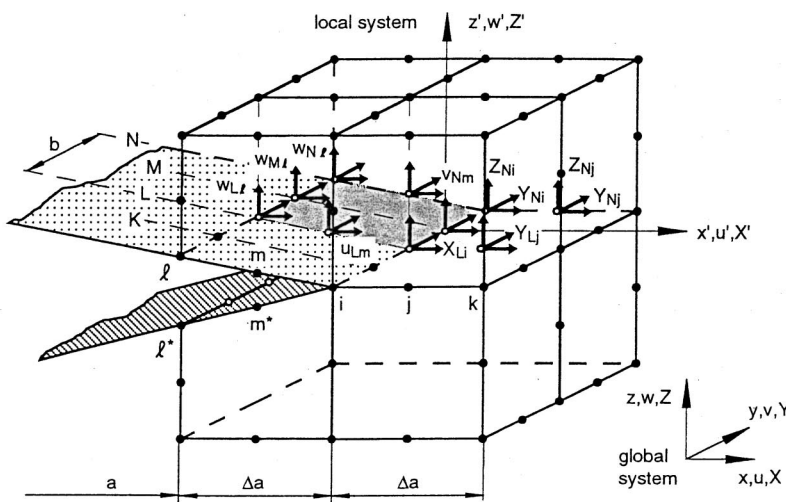
(a). 3D view (lower surface forces are omitted for clarity)
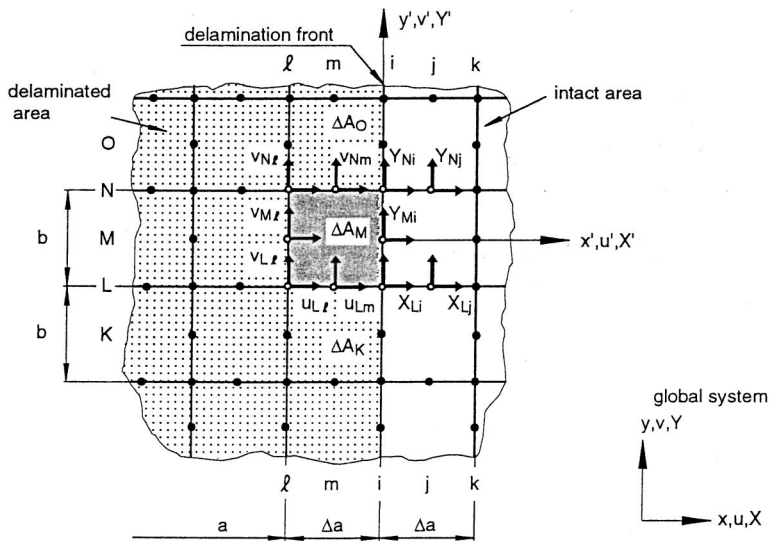
(b). Top view of upper surface (lower surface terms are omitted for clarity)

Fig. 12   Virtual crack closure technique for midside nodes in eight-noded plate/shell and twenty-noded solid elements. a) 3D view (lower surface forces are omitted for clarity) and b) top view of upper surface (lower surface terms are omitted for clarity).

which may be advantageous in cases where the elements are not of square or rectangular shape. For example, for the computation of the strain energy release rate components along a circular or elliptical front where elements are trapezoidal the user may find this approach more suitable. The equations to calculate the strain energy release rate components for one element as shown in Fig. 13 are as follows [66–68]:

$$G_I = -\frac{1}{2\Delta A_M}[Z_{Li}(w_{L\ell}-w_{L\ell*})+Z_{Lj}(w_{Lm}-w_{Lm*})$$

$$+Z_{Mi}(w_{M\ell}-w_{M\ell*})+Z_{Ni}(w_{N\ell}-w_{N\ell*})$$

$$+Z_{Nj}(w_{Nm}-w_{Nm*})], \tag{20}$$

$$G_{II} = -\frac{1}{2\Delta A_M}[X_{Li}(u_{L\ell}-u_{L\ell*})+X_{Lj}(u_{Lm}-u_{Lm*})$$

$$+X_{Mi}(u_{M\ell}-u_{M\ell*})+X_{Ni}(u_{N\ell}-u_{N\ell*})$$

$$+X_{Nj}(u_{Nm}-u_{Nm*})], \tag{21}$$

$$G_{III} = -\frac{1}{2\Delta A_M}[Y_{Li}(v_{L\ell}-v_{L\ell*})+Y_{Lj}(v_{Lm}-v_{Lm*})$$

$$+Y_{Mi}(v_{M\ell}-v_{M\ell*})+Y_{Ni}(v_{N\ell}-v_{N\ell*})$$

$$+Y_{Nj}(v_{Nm}-v_{Nm*})], \tag{22}$$

where the forces at locations Li, Lj and Ni, Nj are calculated only from elements A and B, which are shaded in Fig. 13(b). This is unlike the previous equations where four elements contributed to the forces at locations Li, Lj and Ni, Nj. The force at location Mi is also calculated from elements A and B, which is identical to the procedure above.

A three-dimensional twenty-noded singular brick element with quarter points is shown in Fig. 14. As mentioned above the desired $1/\sqrt{r}$ singularity of the stress field at the crack tip is achieved by moving the midside node to the quarter position. A prism-shaped singular element is obtained by collaps-
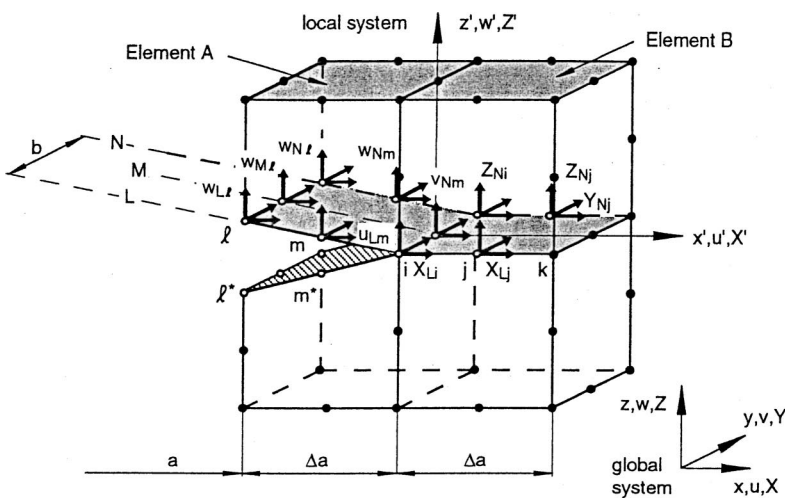
(a). 3D view (lower surface forces are omitted for clarity)
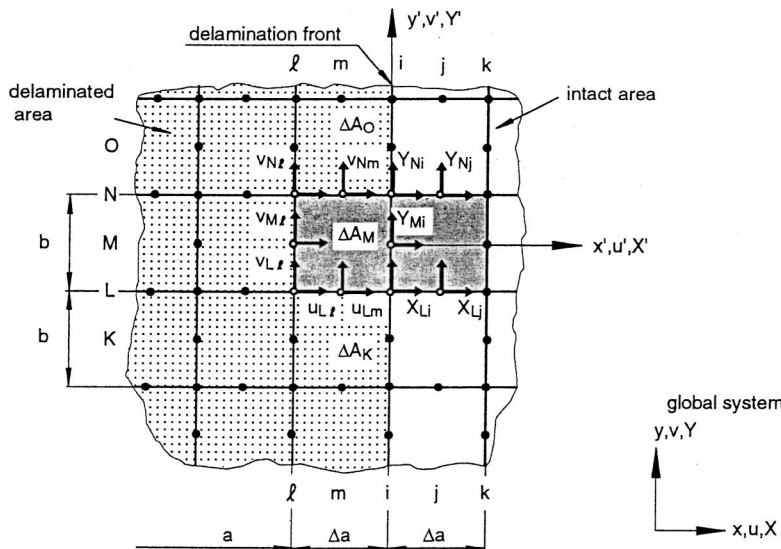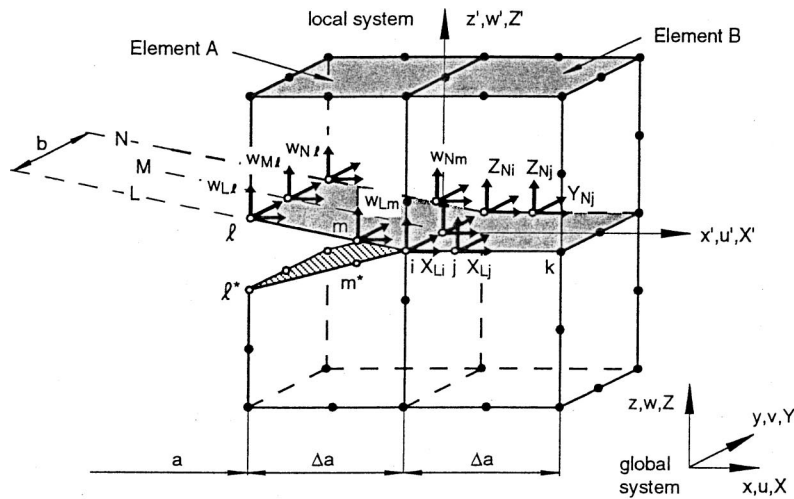

(b). Top view of upper surface (lower surface terms are omitted for clarity)

Fig. 13   Virtual crack closure technique (element method) for eight-noded plate/shell and twenty-noded solid elements. a) 3D view (lower surface forces are omitted for clarity) and b) top view of upper surface (lower surface terms are omitted for clarity).

ing a face of the element as shown in Fig. 15. Each set of collapsed nodes at the front must either be defined as a single node or the degrees of freedom must be connected through multipoint constraints as if each set was a single node. The mode I, mode II, and mode III components of the strain energy release rate, G_I, G_{II}, and G_{III}, are calculated for a brick or prism singularity element using the simplified equations given in Ref. [68]:

$$
\begin{aligned}
G_I = -\frac{1}{2\Delta A_M}\Bigg[&Z_{Li}\Big\{ t_{11}(w_{Lm}-w_{Lm*})+t_{12}(w_{M\ell}-w_{M\ell*})-2t_{12}(w_{L\ell}-w_{L\ell*})-\frac{t_{12}}{2}(w_{N\ell}-w_{N\ell*})\Big\} \\
&+Z_{Ni}\Big\{ t_{12}(w_{M\ell}-w_{M\ell*})-\frac{t_{12}}{2}(w_{L\ell}-w_{L\ell*})-2t_{12}(w_{N\ell}-w_{N\ell*})+t_{11}(w_{Nm}-w_{Nm*})\Big\} \\
&+Z_{Nj}\Big\{ \frac{1}{2}(w_{N\ell}-w_{N\ell*})+(w_{Nm}-w_{Nm*})\Big\}+Z_{Mi}\Big\{ \frac{t_{11}}{2}(w_{Lm}-w_{Lm*})+t_{21}(w_{M\ell}-w_{M\ell*})+t_{22}(w_{N\ell}-w_{N\ell*}) \\
&+t_{22}(w_{L\ell}-w_{L\ell*})+\frac{t_{11}}{2}(w_{Nm}-w_{Nm*})\Big\}+Z_{Lj}\Big\{ (w_{Lm}-w_{Lm*})+\frac{1}{2}(w_{L\ell}-w_{L\ell*})\Big\}\Bigg],
\end{aligned}
\tag{23}
$$

(a). *3D view (lower surface forces are omitted for clarity)*
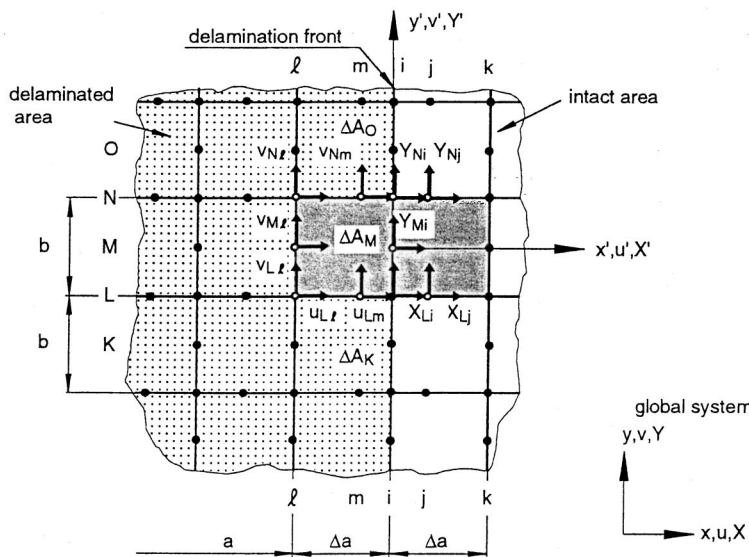
(b). *Top view of upper surface (lower surface terms are omitted for clarity)*

Fig. 14   Virtual crack closure technique (element method) for twenty-noded quarter point elements. *a*) 3D view (lower surface forces are omitted for clarity) and *b*) top view of upper surface (lower surface terms are omitted for clarity).

$$G_{\text{II}} = -\frac{1}{2\Delta A_M}\left[X_{Li}\left\{t_{11}(u_{Lm}-u_{Lm*})+t_{12}(u_{M\ell}-u_{M\ell*})\right.\right.$$

$$\left.-2t_{12}(u_{L\ell}-u_{L\ell*})-\frac{t_{12}}{2}(u_{N\ell}-u_{N\ell*})\right\}$$

$$+X_{Ni}\left\{t_{12}(u_{M\ell}-u_{M\ell*})-\frac{t_{12}}{2}(u_{L\ell}-u_{L\ell*})-2t_{12}(u_{N\ell}-u_{N\ell*})+t_{11}(u_{Nm}-u_{Nm*})\right\}$$

$$+X_{Nj}\left\{\frac{1}{2}(u_{N\ell}-u_{N\ell*})+(u_{Nm}-u_{Nm*})\right\}+X_{Mi}\left\{\frac{t_{11}}{2}(u_{Lm}-u_{Lm*})+t_{21}(u_{M\ell}-u_{M\ell*})\right.$$

$$\left.\left.+t_{22}(u_{N\ell}-u_{N\ell*})+t_{22}(u_{L\ell}-u_{L\ell*})+\frac{t_{11}}{2}(u_{Nm}-u_{Nm*})\right\}+X_{Lj}\left\{(u_{Lm}-u_{Lm*})+\frac{1}{2}(u_{L\ell}-u_{L\ell*})\right\}\right], \qquad (24)$$
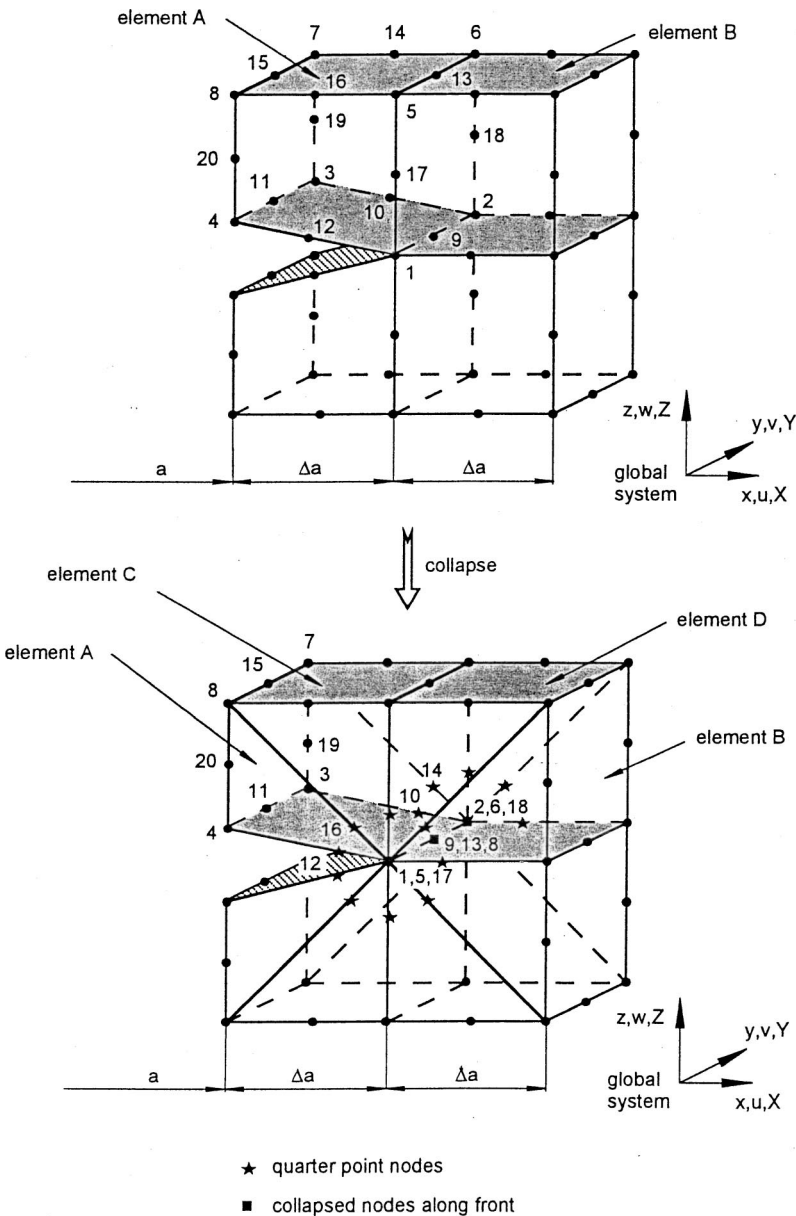

Fig. 15   Collapsed twenty-noded solid singularity elements with quarter point nodes at crack tip

$$
\begin{aligned}
G_{\mathrm{III}} = -\frac{1}{2\Delta A_M}\Bigg[& Y_{Li}\Big\{ t_{11}(v_{Lm}-v_{Lm*})+t_{12}(v_{M\ell}-v_{M\ell*})-2t_{12}(v_{L\ell}-v_{L\ell*})-\frac{t_{12}}{2}(v_{N\ell}-v_{N\ell*})\Big\} \\
& +Y_{Ni}\Big\{ t_{12}(v_{M\ell}-v_{M\ell*})-\frac{t_{12}}{2}(v_{L\ell}-v_{L\ell*})-2t_{12}(v_{N\ell}-v_{N\ell*})+t_{11}(v_{Nm}-v_{Nm*})\Big\} \\
& +Y_{Nj}\Big\{ \frac{1}{2}(v_{N\ell}-v_{N\ell*})+(v_{Nm}-v_{Nm*})\Big\}+Y_{Mi}\Big\{ \frac{t_{11}}{2}(v_{Lm}-v_{Lm*})+t_{21}(v_{M\ell}-v_{M\ell*}) \\
& +t_{22}(v_{N\ell}-v_{N\ell*})+t_{22}(v_{L\ell}-v_{L\ell*})+\frac{t_{11}}{2}(v_{Nm}-v_{Nm*})\Big\}+Y_{Lj}\Big\{(v_{Lm}-v_{Lm*})+\frac{1}{2}(v_{L\ell}-v_{L\ell*})\Big\}\Bigg],
\end{aligned}
\tag{25}
$$

where

$$t_{11}=6\pi-20,\quad t_{12}=\pi-4,\quad t_{21}=\pi-2,$$

$$t_{22}=-\frac{5\pi}{4}+4.\tag{26}$$

As mentioned in the section for regular twenty-noded brick elements, the forces at locations Li, Lj and Ni, Nj as well as Mi are calculated only from elements A and B, which are shaded in Fig. 14(b). In contrast to Eqs. (20)–(22) for regular brick elements, Eqs. (23)–(25) for the quarter-point elements have cross terms involving the corner and quarter-point forces and the relative displacements at the corner and

(a). 3D view (lower surface forces are omitted for clarity)

(b). Top view of upper surface (lower surface terms are omitted for clarity)

Fig. 16   Virtual crack closure technique for four-noded plate/shell elements. a) 3D view (lower surface forces are omitted for clarity) and b) top view of upper surface (lower surface terms are omitted for clarity).

quarter-point nodes. Note that, for the prism element, the nodal forces have to be calculated from elements A, B, C, and D around the crack tip as shown in Fig. 15. A three-dimensional quarter-point brick element with 27 nodes is discussed in Ref. [23]. Additional information with respect to different equations for solid elements are given in Refs. [22],[68–73].

3.2.2 Formulas for plate/shell elements

The use of four-noded plate elements to calculate the mixed-mode strain energy release was demonstrated in Ref. [69]. Equations for the use of VCCT in conjunction with four- and nine-noded plate elements were derived by Wang and Raju [74]. Two techniques to tie the nodes at the delamination front (row i in Figs. 16 and 17) were discussed. For nodes of the upper and lower surfaces, which are joined at the crack tip, the first method enforced the compatibility of translational and rotational degrees of freedom for nodes with identical coordinates. In the second technique, only the compatibility of the translational degrees of freedom were enforced. The second technique allowed the nodes to have independent rotations. For the configurations and loads considered, the second technique appeared to provide preferable constraints,

yielding accurate strain energy release rates [74–76]. Therefore only the equations for this method are mentioned in this paper.

For the four-noded rectangular plate element, as shown in Fig. 16, the equations to calculate the strain energy release rate components at the element corner nodes (location Li) are

$$G_{\mathrm{I}}=-\frac{1}{2\Delta A}Z_{Li}(w_{L\ell}-w_{L\ell*}), \tag{27}$$

$$G_{\mathrm{II}}=-\frac{1}{2\Delta A}X_{Li}(u_{L\ell}-u_{L\ell*}), \tag{28}$$

$$G_{\mathrm{III}}=-\frac{1}{2\Delta A}Y_{Li}(v_{L\ell}-v_{L\ell*}), \tag{29}$$

where $\Delta A=\Delta a(b_{1}+b_{2})/2$ is the crack surface closed as shown in Fig. 16(b) [74].

The equations to calculate the strain energy release rate components for a nine-noded plate element as shown in Fig. 17 are, for the mode I components,
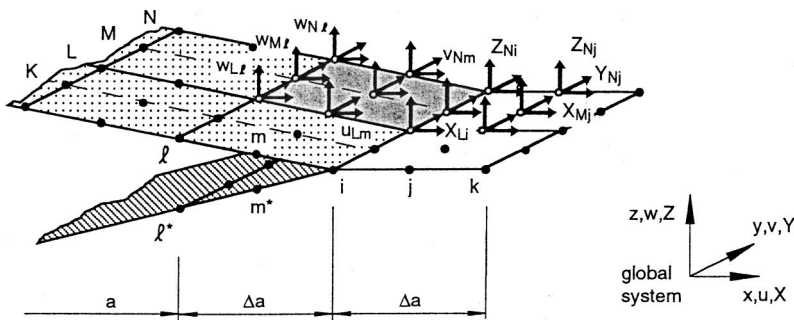
(a). *3D view (lower surface forces are omitted for clarity)*
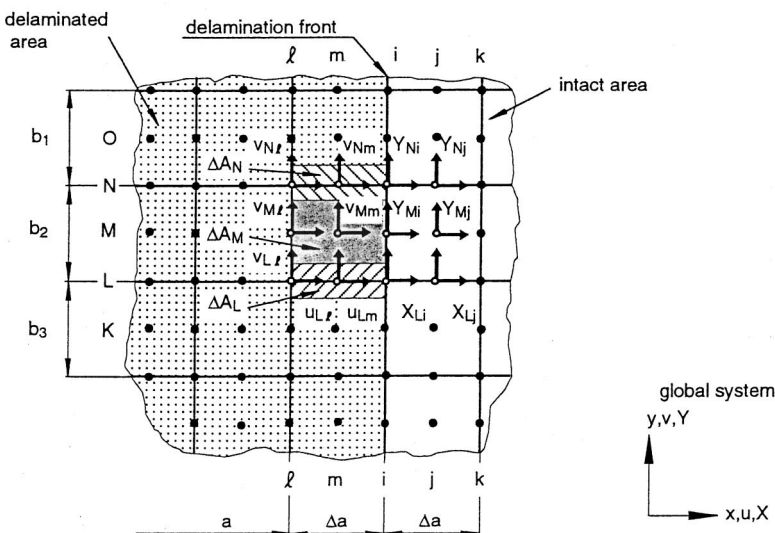
(b). *Top view of upper surface (lower surface terms are omitted for clarity)*
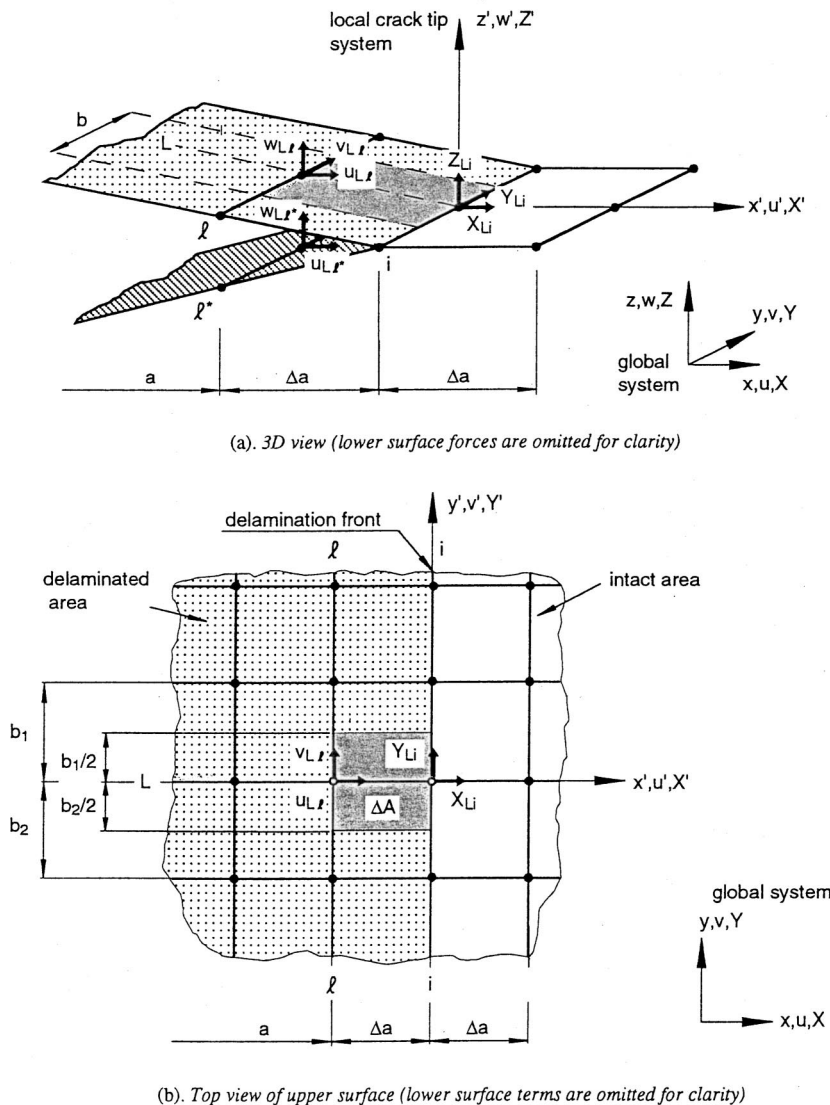
Fig. 17 Virtual crack closure technique for nine-noded plate/shell elements. *a*) 3D view (lower surface forces are omitted for clarity) and *b*) top view of upper surface (lower surface terms are omitted for clarity).

$$G_\mathrm{I}|_L = -\frac{1}{2\Delta A_L}[Z_{Li}(w_{L\ell}-w_{L\ell*})+Z_{Lj}(w_{Lm}-w_{Lm*})],$$

(30)

$$G_\mathrm{I}|_M = -\frac{1}{2\Delta A_M}[Z_{Mi}(w_{M\ell}-w_{M\ell*})$$
$$+Z_{Mj}(w_{Mm}-w_{Mm*})],$$

(31)

$$G_\mathrm{I}|_N = -\frac{1}{2\Delta A_N}[Z_{Ni}(w_{N\ell}-w_{N\ell*})+Z_{Nj}(w_{Nm}-w_{Nm*})],$$

(32)

mode II components,

$$G_\mathrm{II}|_L = -\frac{1}{2\Delta A_L}[X_{Li}(u_{L\ell}-u_{L\ell*})+X_{Lj}(u_{Lm}-u_{Lm*})],$$

(33)

$$G_\mathrm{II}|_M = -\frac{1}{2\Delta A_M}[X_{Mi}(u_{M\ell}-u_{M\ell*})$$
$$+X_{Mj}(u_{Mm}-u_{Mm*})],$$

(34)

$$G_\mathrm{II}|_N = -\frac{1}{2\Delta A_N}[X_{Ni}(u_{N\ell}-u_{N\ell*})+X_{Nj}(u_{Nm}-u_{Nm*})],$$

(35)

and mode III components,

$$G_\mathrm{III}|_L = -\frac{1}{2\Delta A_L}[Y_{Li}(v_{L\ell}-v_{L\ell*})+Y_{Lj}(v_{Lm}-v_{Lm*})],$$

(36)

$$G_\mathrm{III}|_M = -\frac{1}{2\Delta A_M}[Y_{Mi}(v_{M\ell}-v_{M\ell*})$$
$$+Y_{Mj}(v_{Mm}-v_{Mm*})],$$

(37)

$$G_\mathrm{III}|_N = -\frac{1}{2\Delta A_N}[Y_{Ni}(v_{N\ell}-v_{N\ell*})+Y_{Nj}(v_{Nm}-v_{Nm*})],$$

(38)

as given in Refs. [74],[75]. Here indices L, M, N denote the column location, as shown in Fig. 17(b) and

$$\Delta A_L = -\tfrac{1}{6}\Delta a(b_2+b_3), \quad \Delta A_M = -\tfrac{2}{3}\Delta ab_2$$
$$\text{and} \quad \Delta A_N = -\tfrac{1}{6}\Delta a(b_1+b_2)$$

(39)

are the equivalent crack surfaces apportioned to corner- and midside-crack front nodes, respectively. The equivalent crack surfaces are obtained by assuming that the strain energy release rate components are constant across the width of an element [74]. For eight-noded plate elements the Mm terms are equal to zero and the equations at column M are reduced to

$$G_\mathrm{I}|_M = -\frac{1}{2\Delta A_M}[Z_{Mi}(w_{M\ell}-w_{M\ell*})],$$

(40)

$$G_\mathrm{II}|_M = -\frac{1}{2\Delta A_M}[X_{Mi}(u_{M\ell}-u_{M\ell*})],$$

(41)

$$G_\mathrm{III}|_M = -\frac{1}{2\Delta A_M}[Y_{Mi}(v_{M\ell}-v_{M\ell*})],$$

(42)

with the equations for columns L and N unaltered.

Built-up structures are traditionally modeled and analyzed using plate or shell finite elements to keep the modeling and computational effort affordable. Computed mixed-mode strain energy release rate components, however, depend on many variables such as element order and shear deformation assumptions, kinematic constraints in the neighborhood of the delamination front, and continuity of material properties and section stiffness in the vicinity of the debond when delaminations or debondings are modeled with plate or shell finite elements [74,75]. For example, in Ref. [75] mesh refinement studies showed that computed G_I, G_II, and G_III did not converge when the structure above and below the plane of delamination was modeled with plate elements with different section properties (thickness or layup). A comparison of computed mixed-mode strain energy release rates obtained from plate models with values computed from 3D models showed differences in results near the free edges of the structure where the stress state is 3D [77]. These problems may be avoided by using 3D models. Furthermore, 3D analyses are required when matrix cracks and multiple delaminations need to be modeled at different ply interfaces. Since many layers of brick elements through the thickness are often necessary to model the individual plies, the size of finite element models required for accurate analyses may become prohibitively large. For future detailed modeling, the shell/3D modeling technique offers great potential for saving modeling and computational effort because only a relatively small section in the vicinity of the delamination front needs to be modeled with solid elements [78].

3.3 Formulas for geometrically nonlinear analysis

For geometric nonlinear analysis where large deformations may occur, both forces and displacements obtained in the global coordinate system need to be transformed into a local coordinate system (x',z') that originates at the crack tip as shown in Fig. 18. The local crack tip system defines the tangential (x', or mode II) and normal (z', or mode I) coordinate directions at the crack tip in the deformed configuration as shown in Fig. 18(b) for the two-dimensional case. The vector through nodes i and k in the deformed configuration defines the local x' direction as shown in Fig. 18(a). The local z' direction, which defines mode I, is perpendicular to the local x' direction, which defines mode II. Forces at node row i and displacements at node row ℓ need to be transformed to the local x'-z' system at the tip as shown in Fig. 18(b). The transformation is required to correctly compute the mixed-mode energy release rates G_I and G_II. The total energy release rate remains unaffected by this transformation. The accuracy of the computed mixed-mode energy release rates depends on the accuracy of the forces and displacements obtained form the nonlinear finite element analysis. The equations to calculate the mixed-mode energy release rate components remain the same as before, with forces

and displacements now expressed in the local system. For the two-dimensional eight-noded quadrilateral element with quadratic shape functions this yields

$$G_{\mathrm{I}} = -\frac{1}{2\Delta a}[Z_i'(w_\ell' - w_{\ell*}') + Z_j'(w_m' - w_{m*}')], \tag{43}$$

$$G_{\mathrm{II}} = -\frac{1}{2\Delta a}[X_i'(u_\ell' - u_{\ell*}') + X_j'(u_m' - u_{m*}')], \tag{44}$$

where X_i', Z_i' and X_j', Z_j' are the forces at the crack tip (nodal point i) and in front of the crack (nodal point j) in the local crack tip system. The relative sliding and opening behind the crack tip are calculated at nodal points ℓ and $\ell*$ from the transformed displacements at the upper crack face u_ℓ' and w_ℓ' and the displacements $u_{\ell*}'$ and $w_{\ell*}'$ at the lower crack face. Additional to the relative displacements at nodal points ℓ and $\ell*$, the relative displacements at nodal points m and $m*$ are required, which are calculated from displacements at the upper crack face u_m' and w_m' and the displacements u_{m*}' and w_{m*}' at the lower crack face. Three-dimensional analysis additionally requires the definition of the tangential (y', or mode III) coordinate direction, which will be discussed in Sec. 3.5.

3.4 Corrections for elements with different lengths or widths at the crack tip

3.4.1 Correcting for elements with different lengths at the crack tip

All equations in previous sections have been derived under the assumption that the element lengths Δa for the element in front of the crack tip and behind are identical. Once automatic mesh generators are used to create complex models, the ideal case of identical element length can no longer be assumed and corrections are required. In their original paper Rybicki and Kanninen [19] use the $1/\sqrt{r}$ singularity of the stress field at the crack tip to derive the corrected equations. A sketch of a crack tip modeled with two-dimensional finite elements of unequal length is shown in Fig. 19. The forces X_i, Z_i at the crack tip (nodal point i) calculated for an element length Δa_2 are known from the finite element analysis.

(a). *Definition of local crack tip coordinate system*

(b). *Forces and displacements in local coordinate system (lower surface forces are omitted for clarity)*
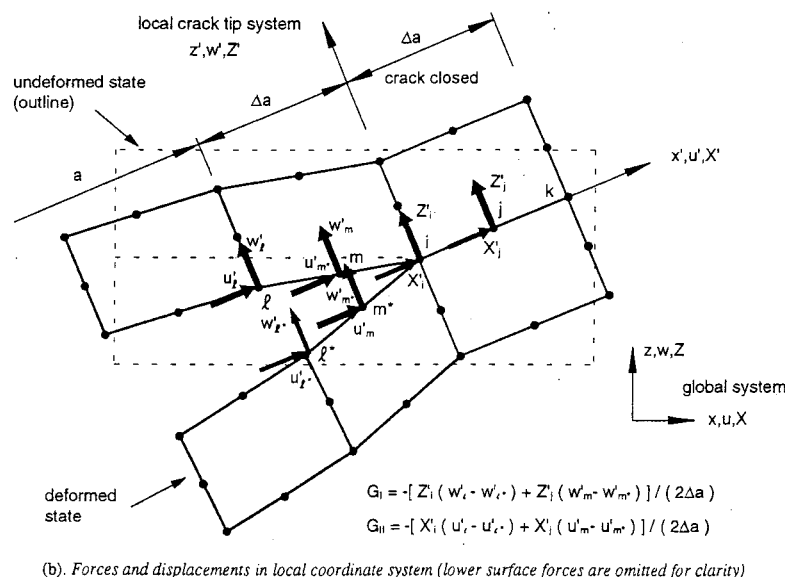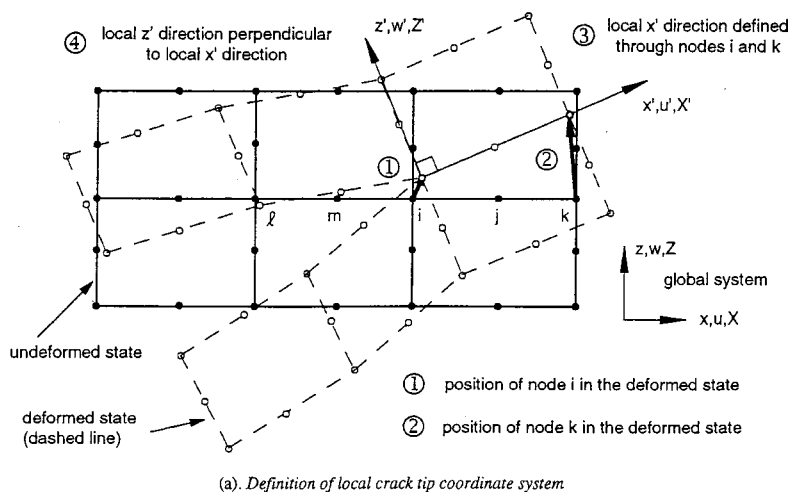
Fig. 18   Virtual crack closure technique for geometrically nonlinear analysis. *a*) Definition of local crack tip coordinate system and *b*) forces and displacements in local coordinate system (lower surface forces are omitted for clarity).

Required for the virtual crack closure technique, however, are the forces $\widetilde{X}_i$, $\widetilde{Z}_i$ matching the relative displacements at node ℓ behind the crack tip, which have been calculated for an element length Δa_1.

The stress tip field at the crack tip can be expressed as [53]

$$\sigma(r) = b\sigma_\infty \frac{1}{\sqrt{r}} = \frac{dX}{dA} = \frac{dX}{bdr}, \tag{45}$$

where b is the element width or thickness, σ_∞ is the undisturbed far field stress, and $\sigma(r)$ is the stress in front of the crack, which is a function of the distance r from the crack tip. The forces at the crack tip for element length Δa_1 and Δa_2 are obtained through integration:

$$\widetilde{X}_i = \int_0^{\Delta a_1} \frac{dr}{r^{1/2}} = 2b\sigma_\infty \Delta a_1^{1/2}, \tag{46}$$

$$X_i = 2b\sigma_\infty \Delta a_2^{1/2}. \tag{47}$$

A relationship between the forces can be derived, which only depends on the length of the elements in front and behind the crack tip

$$\widetilde{X}_i = \left(\frac{\Delta a_1}{\Delta a_2}\right)^{1/2} X_i. \tag{48}$$

The calculation of the crack opening force $\widetilde{Z}_i$ is done accordingly. With the relationship of the forces established, the required forces $\widetilde{X}_i$, $\widetilde{Z}_i$ may be substituted with the forces X_i, Z_i obtained from finite element analysis, yielding the corrected equations for the energy release rate components

$$G_{\mathrm{I}} = -\frac{1}{2\Delta a_1} Z_i (w_\ell - w_{\ell*}) \left(\frac{\Delta a_1}{\Delta a_2}\right)^{1/2}, \tag{49}$$

$$G_{\mathrm{II}} = -\frac{1}{2\Delta a_1} X_i (u_\ell - u_{\ell*}) \left(\frac{\Delta a_1}{\Delta a_2}\right)^{1/2}. \tag{50}$$
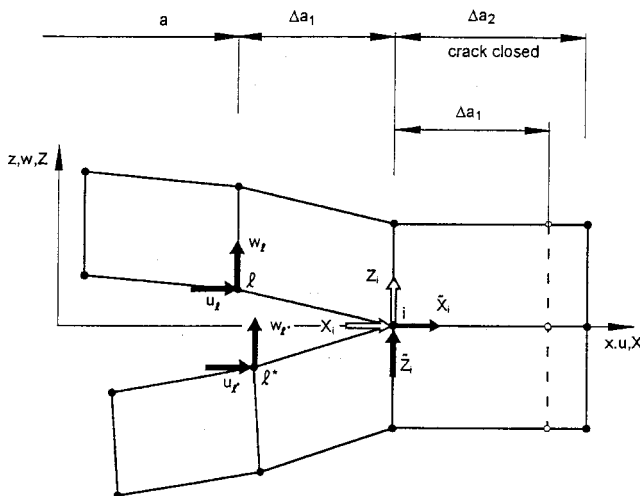

Fig. 19   Correction for elements with different lengths in front and behind the crack tip

A different approach for correcting the equations, which does not depend on the assumption of the $1/\sqrt{r}$ singularity of the stress field at the crack tip, is depicted in Fig. 20 for the 2D case. The different element lengths are accounted for by correcting the displacements behind the crack tip (at node ℓ), which were computed for a length Δa_1, to match the forces X_i, Z_i at the crack tip (nodal point i), which were computed for an element length Δa_2. The displacements are adjusted by taking into account the shape functions of the elements or approximated by simple linear interpolation. For elements with linear shape functions, where the displacement varies linearly along the element edge, both methods are identical. The displacement at locations $\widetilde{\ell}$ and $\widetilde{\ell}*$ are calculated using a linear interpolation for $\Delta a_1 > \Delta a_2$ as shown in Fig. 20(a) and linear extrapolation is used for $\Delta a_1 < \Delta a_2$ as shown in Fig. 20(b) yielding

$$u_{\widetilde{\ell}} = u_\ell \frac{\Delta a_2}{\Delta a_1}, \qquad u_{\widetilde{\ell}*} = u_{\ell*} \frac{\Delta a_2}{\Delta a_1}. \tag{51}$$

The calculation of the crack opening displacement w is done accordingly. With the relationship of the displacements established, the required displacements at locations $\widetilde{\ell}$ and $\widetilde{\ell}*$ may be substituted with the displacements ℓ and $\ell*$ obtained directly from finite element analysis, yielding the corrected equations for the energy release rate components:

$$G_{\mathrm{I}} = -\frac{1}{2\Delta a_2} Z_i (w_\ell - w_{\ell*}) \frac{\Delta a_2}{\Delta a_1}, \tag{52}$$

$$G_{\mathrm{II}} = -\frac{1}{2\Delta a_2} X_i (u_\ell - u_{\ell*}) \frac{\Delta a_2}{\Delta a_1}. \tag{53}$$

The method first described imposes an analytical relationship based on the $1/\sqrt{r}$ singularity of the stress field at the crack tip. However, the second method is less restrictive because the results only depend on the finite element discretization at the crack tip.

3.4.2 Correcting for elements with different widths along the delamination front

For the derivation of the equations in the previous sections it had been assumed that the front is straight and that element widths b remain constant along the front. Meshing of arbitrarily shaped delamination front contours will, however, cause element length Δa and width b to vary along the front. Therefore, a two-dimensional representation of a crack or delamination in a plate/shell or a 3D solid finite element models also requires a correction accounting for differences in element widths b along the front. For components modeled with four-noded plate/shell type elements or eight-noded solid brick elements the correction is straightforward as shown in Fig. 21. A variation of only the element length, Δa, yields equations equivalent to the 2D case discussed earlier:

$$G_\text{I}=-\frac{1}{2\Delta a_2 b}Z_{Li}(w_{L\ell}-w_{L\ell*})\frac{\Delta a_2}{\Delta a_1}, \tag{54}$$

$$G_\text{II}=-\frac{1}{2\Delta a_2 b}X_{Li}(u_{L\ell}-u_{L\ell*})\frac{\Delta a_2}{\Delta a_1}, \tag{55}$$

$$G_\text{III}=-\frac{1}{2\Delta a_2 b}Y_{Li}(v_{L\ell}-v_{L\ell*})\frac{\Delta a_2}{\Delta a_1}. \tag{56}$$

The additional variation of the element width b requires the separate calculation of the contributing element surfaces $\Delta A_1=\frac{1}{2}\Delta a_2 b_1$ and $\Delta A_2=\frac{1}{2}\Delta a_2 b_2$, yielding the corrected equations for the energy release rate components

$$G_\text{I}=-\frac{1}{2}\frac{1}{\Delta A_1+\Delta A_2}Z_{Li}(w_{L\ell}-w_{L\ell*})\frac{\Delta a_2}{\Delta a_1}, \tag{57}$$

$$G_\text{II}=-\frac{1}{2}\frac{1}{\Delta A_1+\Delta A_2}X_{Li}(u_{L\ell}-u_{L\ell*})\frac{\Delta a_2}{\Delta a_1}, \tag{58}$$

$$G_\text{III}=-\frac{1}{2}\frac{1}{\Delta A_1+\Delta A_2}Y_{Li}(v_{L\ell}-v_{L\ell*})\frac{\Delta a_2}{\Delta a_1}. \tag{59}$$

A simple equivalent expression for twenty-noded solid brick elements based on the equations presented in Sec. 3.2.1 is not available. The set of equations given in Sec. 3.2.2 for the higher-order plate elements [74] may be used since the change of element width is already accounted for in the expressions for the mixed-mode strain energy release rates. The variation in element length, Δa, may be compensated as described in the preceding section.
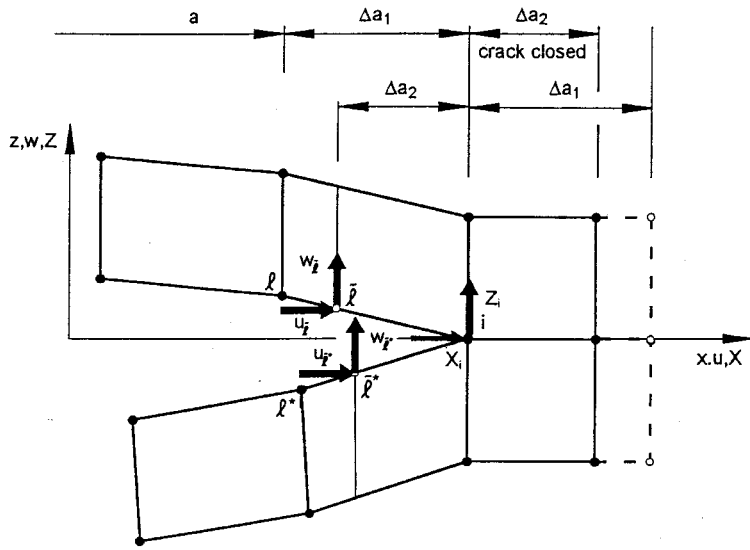
(a) Shorter elements in front of the crack tip
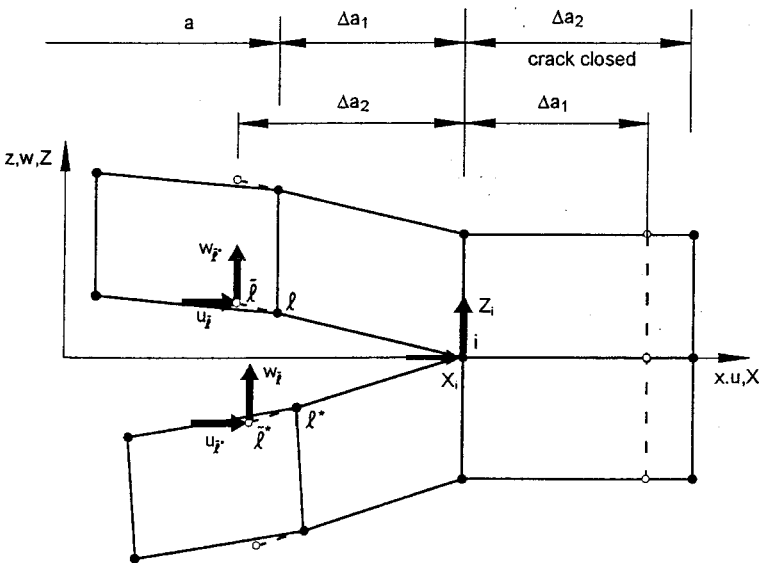
(b) Longer elements in front of the crack tip .

Fig. 20   Correction for elements with different lengths in front and behind the crack tip. a) Shorter elements in front of the crack tip and b) longer elements in front of the crack tip.
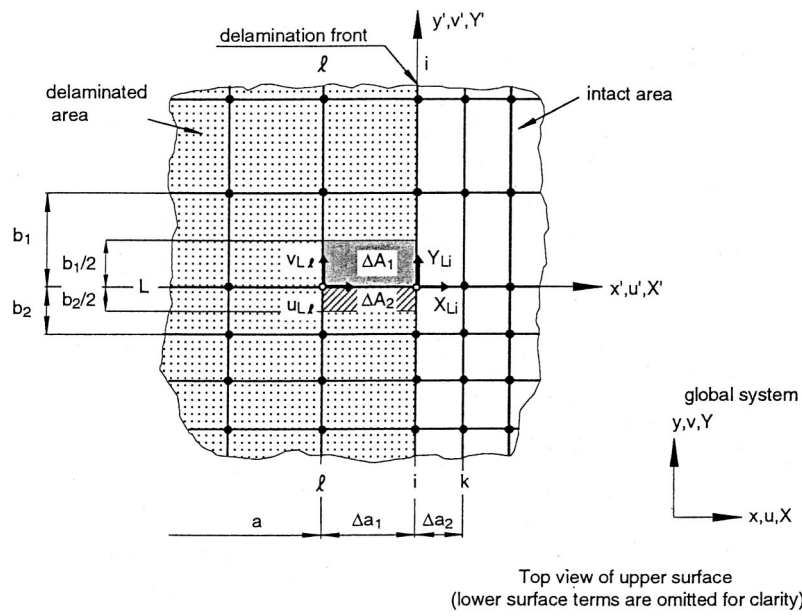
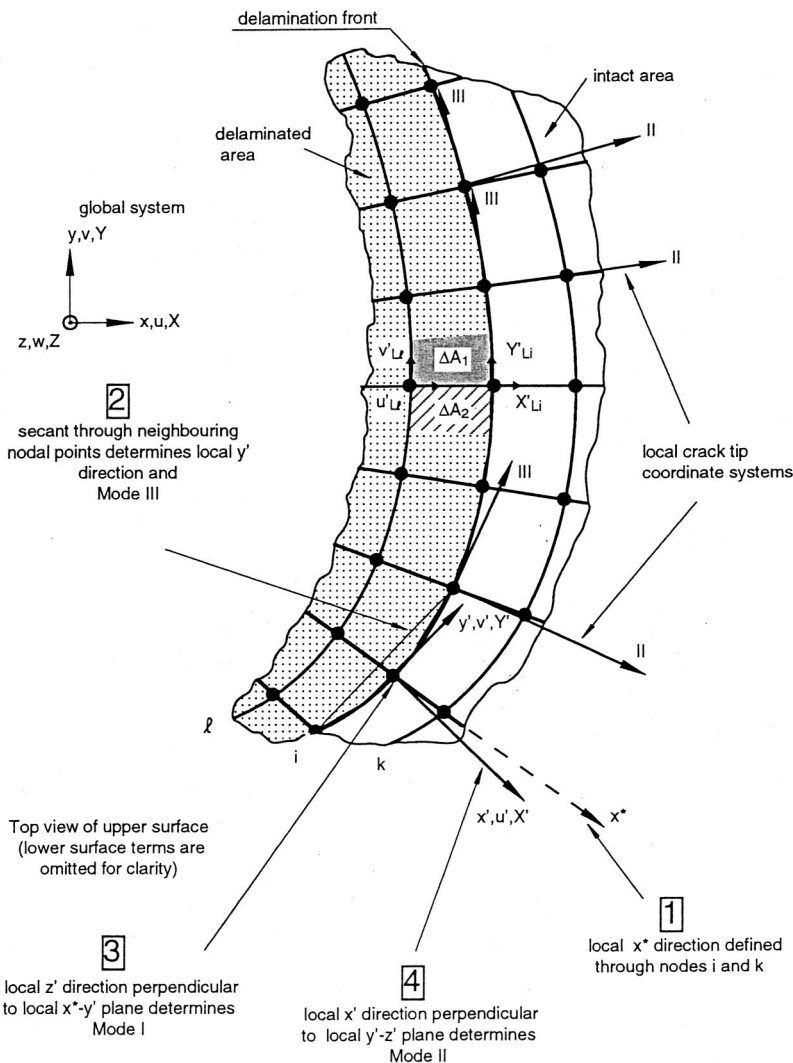Fig. 21   Virtual crack closure technique for eight-noded solid elements with different widths

Fig. 22   Virtual crack closure technique for arbitrarily shaped front

3.5 Procedures for arbitrarily shaped delamination front contours

The equations presented in the previous sections were derived with the assumption that the delamination front is straight. For a straight front as shown in Figs. 10–17 and 21 the definition of the modes is intuitive and constant for the entire front: Mode I is caused by the out of plane crack opening, mode II by the shear perpendicular to the straight delamination/crack front, and mode III by the shear component tangential to the front. For an arbitrarily shaped front the mode definition constantly changes along the contour as shown in Fig. 22. A local crack tip coordinate system therefore needs to be defined at each nodal point along the front [79]. The vector through nodes i and k in the deformed configuration defines the local x^* direction as shown for one sample node in Fig. 22. The secant through adjacent nodes defines the y' direction and mode III. The local plane of delamination is defined by x^* and y'. The local z' direction, which defines mode I, is perpendicular to the plane of delamination. Finally, the local x' direction, which defines mode II, is perpendicular to the y' and z' plane. Forces at node row i and displacements at node row ℓ need to be transformed to the local x'-y'-z' system at the tip. The

transformed forces and displacements are used in the previously derived equations to calculate the mixed-mode energy release rates.

For the procedure described above it is assumed that the mesh remains normal to the delamination front. Modern preprocessing software allows the modeling of almost any complex configuration; these programs, however, were not developed to guarantee the normality of the mesh and the delamination front. The effect of a lack of normality at the crack front on the computed energy release rates was studied in Ref. [80]. It was shown that the standard formulations for VCCT were not able to extract accurate values from models that did not have normality at the crack front when compared to reference solutions. It was also found that an increased variation from the normal condition yielded a greater discrepancy. The formulation of an extraction method for VCCT that yields accurate energy release rates for models that lack normality is given in Ref. [80].

3.6 Suggested solutions for delaminations with sharp corners

Delaminations with sharp corners—as shown in Fig. 23(a)—pose a problem when computing mixed-mode energy release rates as the separation into in-plane shear (mode II) and tearing (mode III) is not defined. Ideally sharp corners generally do not exist so that modeling a rounded corner, as shown in Fig. 23(b), appears to be an acceptable alternative. The mode separation is well defined at the rounded corner and the procedure described in the preceding section may be applied to define the appropriate local crack tip coordinate system.

The method suggested has been applied successfully to a specimen with an embedded, square delamination as shown in Fig. 24 [81]. The method results in an increase of nodes and elements and the model may become large. A recently suggested modified approach uses stair stepped instead of smoothed fronts and thus avoids an increase in model size [82].
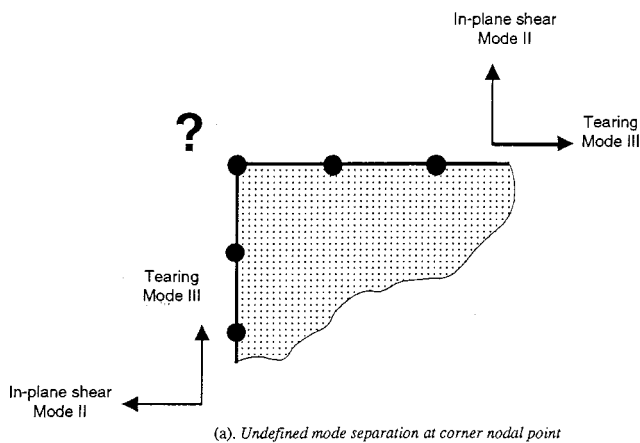
(a). *Undefined mode separation at corner nodal point*
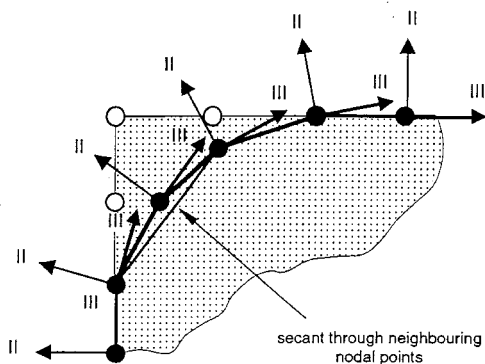
(b). *Well defined mode separation at rounded corner.*

Fig. 23   Definition of mode separation at sharp corners. *a*) Undefined mode separation at corner nodal point and *b*) well-defined mode separation at rounded corner.

Fig. 24   Detail of a finite element mesh with modeled square insert

4 DEALING WITH THE PROBLEMS AT A BIMATERIAL INTERFACE

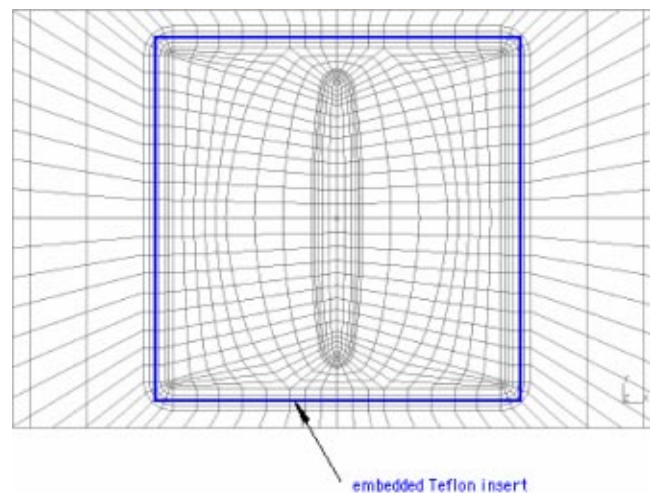Previous investigations have shown that care must be exercised in interpreting the values for G_I, G_{II}, and G_{III} obtained using the virtual crack closure technique for interfacial delaminations between two orthotropic solids [83–86]. Mathematical solutions of the near crack tip field indicate that stresses start to oscillate in the immediate vicinity of the tip when crack growth occurs at interfaces between materials with dissimilar properties as shown in Fig. 25(*a*). The fact that the mixed-mode ratio is undefined when the virtual crack closure length Δa goes to zero has been associated with these stress oscillations near the crack tip. For crack growth and delamination propagation in composite materials, this phenomenon has to be considered as the delamination is

rarely located at an interface between two plies of identical orientation. One way to circumvent this problem is the introduction of an artificial thin resin rich layer that is assumed to exist between the plies [83,87]. Delamination propagation in this case occurs in a homogenious material and the above-mentioned problem does not exist. Although this technique circumvents the issue, it requires larger models with significant refinement in the thin resin layer. Several other papers have addressed the problems of a bimaterial interface and the associated stress oscillations near the crack tip in the past [88–98].

It was shown in the literature [84] that finite values for the virtual crack closure length, eg, $\Delta a/a > 0.05$ (Δa is the virtual crack closure length and a the crack length), result in nearly constant mixed-mode ratios. In addition it was veri-

(a). *Bimaterial Interface*

Δa: element length
h: ply thickness

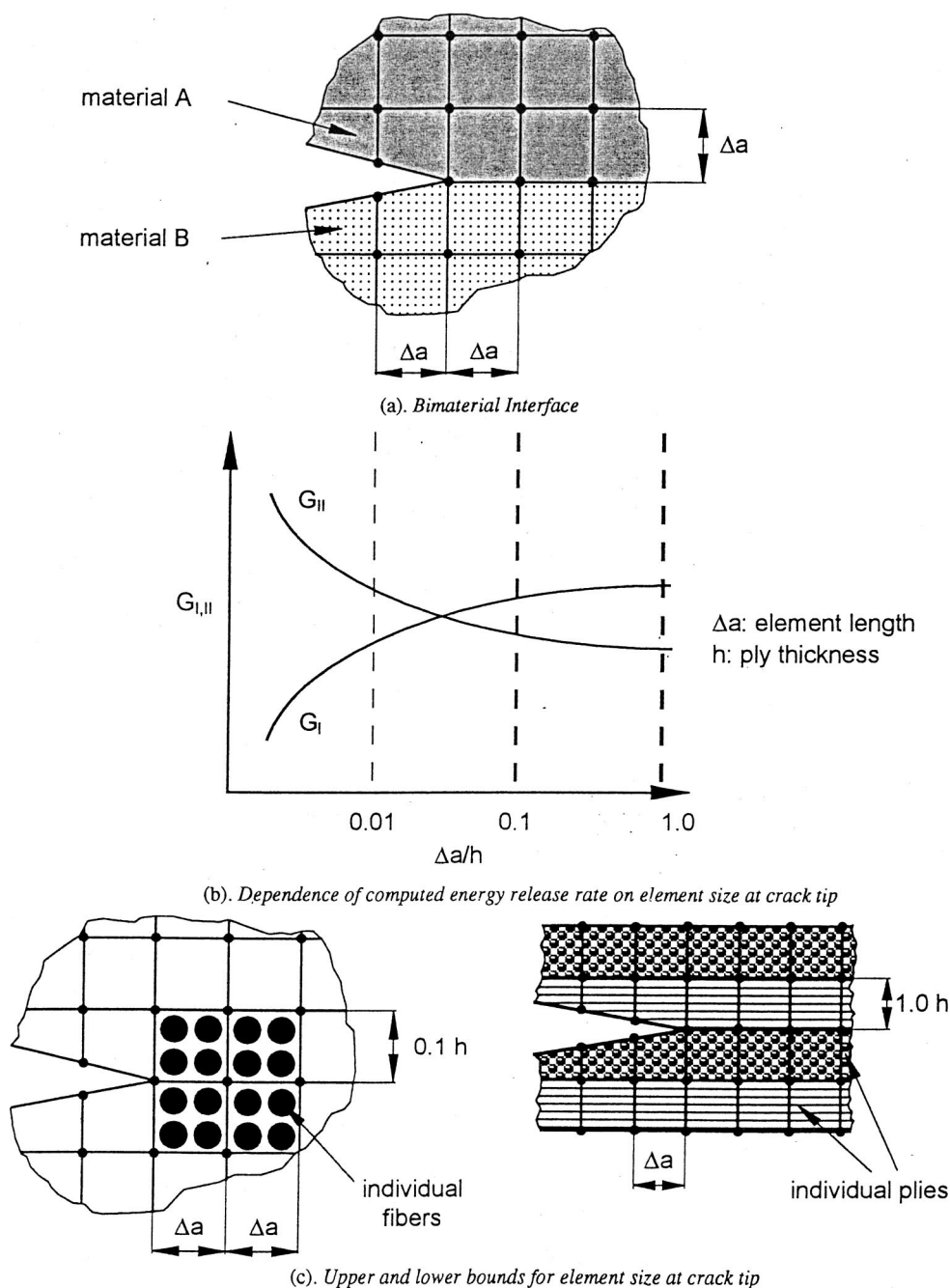(b). *Dependence of computed energy release rate on element size at crack tip*

Fig. 25 Bimaterial interface. *a*) Bimaterial interface, *b*) dependence of computed energy release rate on element size at crack tip and *c*) upper and lower bounds for element size at crack tip.

(c). *Upper and lower bounds for element size at crack tip*

Table 1.   Dependence of mixed-mode ratio in bimaterial interface on element size at the crack tip[a]

Element length Δa (mm)	Relative element size $\Delta a/h$	Relative crack closure length $\Delta a/a$	Mode ratio G_{II}/G_T	Mode ratio G_{III}/G_T
0.062 5	0.492	0.001 969	0.920 48	0.079 509
0.031 25	0.246	0.000 984	0.920 45	0.079 548
0.015 625	0.123	0.000 492	0.920 20	0.079 792
0.078 125	0.061 5	0.000 246	0.915 74	0.084 262
0.003 906 25	0.030 7	0.000 123	0.915 62	0.084 377

[a]Layup $[\pm 30/-30/30/-30/30/30/-30/30/-30/-30/30/_\uparrow-30/30/30/-30/30/-30/-30/30/-30/30/\pm 30]$,
C12K/R6376 tape, delamination length $a = 31.75$ mm, ply thickness $h = 0.127$ mm.

fied in Refs. [85],[86] that evaluating the energy release rates via nodal forces and displacements in the finite element procedure yields results similar to the analytical evaluation of the crack closure integral based on the near tip fields. For larger values of Δa the energy release rate components were found to be nearly constant, whereas for very small Δa they are functions of element length as sketched in Fig. 25(b). The total energy release $G_T = G_I + G_{II} + G_{III}$, however, converges to a constant value as shown in Ref. [75]. The $\Delta a/a$ values where the oscillation begins is connected with the value of γ found in the expression for the crack tip singularity, which is given by $r^{-1/2+i\gamma}$. It was also shown that evaluating energy release rates by using larger values of $\Delta a/a$, where the energy release rate components become stationary, yields similar results to values obtained by an analysis performed assuming a resin-rich region mentioned above [83]. However, the energy release rates evaluated with a larger Δa are insensitive to material inhomogeneities that exist. This is a prerequisite for an energy release rate that is to be used as fracture criterion in a real situation.

For the virtual crack closure technique, the energy release rates are defined as the virtual crack closure integral over a finite crack closure length. This crack closure length corresponds to the lengths of the elements adjacent to the crack front. This element length, Δa, must be chosen small enough to ensure a converged FE solution but large enough to avoid oscillating results. The approach used must be consistent when the definition of the energy release rates used for fracture predictions as well as that employed for material characterization. This does not imply that the material tests must be evaluated by FE models, but it should be established that the data reduction scheme is in agreement with the definition of a finite crack closure length. Consequently, it had been suggested to use element lengths at the crack tip in such a manner that the computed results are insensitive to the variation of the element length Δa at the crack tip as sketched in Fig. 25(b).

Upper and lower bounds may be assumed for practical applications as shown in Fig. 25(c). The element size (length and height) should not be less than $\frac{1}{10}$ of a ply thickness, h, which corresponds to the diameter of two carbon *tows* in the carbon/epoxy material modeled as shown in Fig. 25(c). For smaller element sizes the assumption of modeling each ply as an orthotropic continuum is no longer valid. The ply thickness was suggested as a practical upper limit for element length and height because larger elements would require smearing of the different layer properties over one element as shown in Fig. 25(c) [99]. Smeared or homogenized properties would result in altered properties at the interface

where the energy release rates are calculated. Variations in mode mixety between these upper and lower bounds are typically very small and should prove acceptable for practical applications.

In a previous investigation, mixed-mode energy release rates were computed for an ENF specimen with multidirectional layup, where the delaminated interface was located between a $+30°$ and $-30°$ ply [100,101]. A study indicated that computed energy release rates G_{II} and G_{III}, do not exhibit a significant variation with mesh refinement as shown in Table 1.

In another study the influence of the mesh size at the delamination tip was investigated for a single leg bending (SLB) specimen with multidirectional layup, where the delaminated interface was located between a $+30°$ and $-30°$ ply [100,102,103]. The three-dimensional model of the SLB specimen is shown in Fig. 26. Along the length of the model, a refined mesh of length c was used in the vicinity of the delamination front. The influence of mesh size on computed mixed-mode strain energy release rates was studied by keeping the length of the refined zone c constant, and increasing the number of elements, n, in this zone as shown in the detail of Fig. 26. The corresponding values of relative element size, $\Delta a/h$, and relative crack closure length, $\Delta a/a$, are given in Table 2. The influence of mesh refinement on the mode I strain energy release rate distribution across the width is moderate and only very long elements ($n = 3$, $\Delta a = c/n = 1$ mm) need to be avoided as shown in Fig. 27. This is confirmed by the mode II and mode III distributions as shown in Figs. 28 and 29 where the mode II strain energy release rate is fairly constant across almost the entire width of the specimen and peaks near the edges accompanied by local mode III contribution. The distribution of the mixed-mode ratio G_I/G_{II} is shown in Fig. 30. For the range studied ($n = 3$ up to 48), there is only a small dependence of computed mixed-mode ratio on element size Δa. The results from the above studies of the multidirectional ENF and SLB specimens confirm the suggestion made earlier for lower bounds ($\Delta a/h > 0.1$) and upper bounds ($\Delta a/h < 1.0$) of element lengths to be used.

5   CONVERSION OF ENERGY RELEASE RATES TO STRESS INTENSITY FACTORS

In metal fracture the stress intensity factor K is commonly used to describe the stress state at the crack tip. A considerable database exists of experimentally determined fracture-toughness values, K_C, obtained for a wide range of materi-

als. It may therefore be desirable to convert computed strain energy release rates G to stress intensity factors K. The assumption of a plane stress condition yields

$$K_I = \sqrt{G_I E}, \tag{60}$$

$$K_{II} = \sqrt{G_{II} E}, \tag{61}$$

while the assumption of a plane strain condition yields

$$K_I = \sqrt{\frac{G_I E}{(1 - \nu^2)}}, \tag{62}$$

$$K_{II} = \sqrt{\frac{G_{II} E}{(1 - \nu^2)}}, \tag{63}$$

$$K_{III} = \sqrt{\frac{G_{III} E}{(1 + \nu)}}, \tag{64}$$

where E is the Young's modulus and ν is the Poisson's ratio [53].

Failure in composite materials is expected when, for a given mixed mode ratio G_{II}/G_T, the calculated total energy release rate G_T exceeds the interlaminar fracture toughness G_c as shown in Fig. 2 for IM7/8552 [14]. Due to the fact that the calculation of stress intensity factors is not necessary for the prediction of delamination onset or growth in composites the lengthy equations required to convert energy release rates to stress intensity factors for orthotropic and anisotropic materials are not given in this paper and the interested reader is referred to the Ref. [104].

– – – – – outline of undeformed configuration
w_c: deflection in the center of the specimen

detail of local model around delamination front

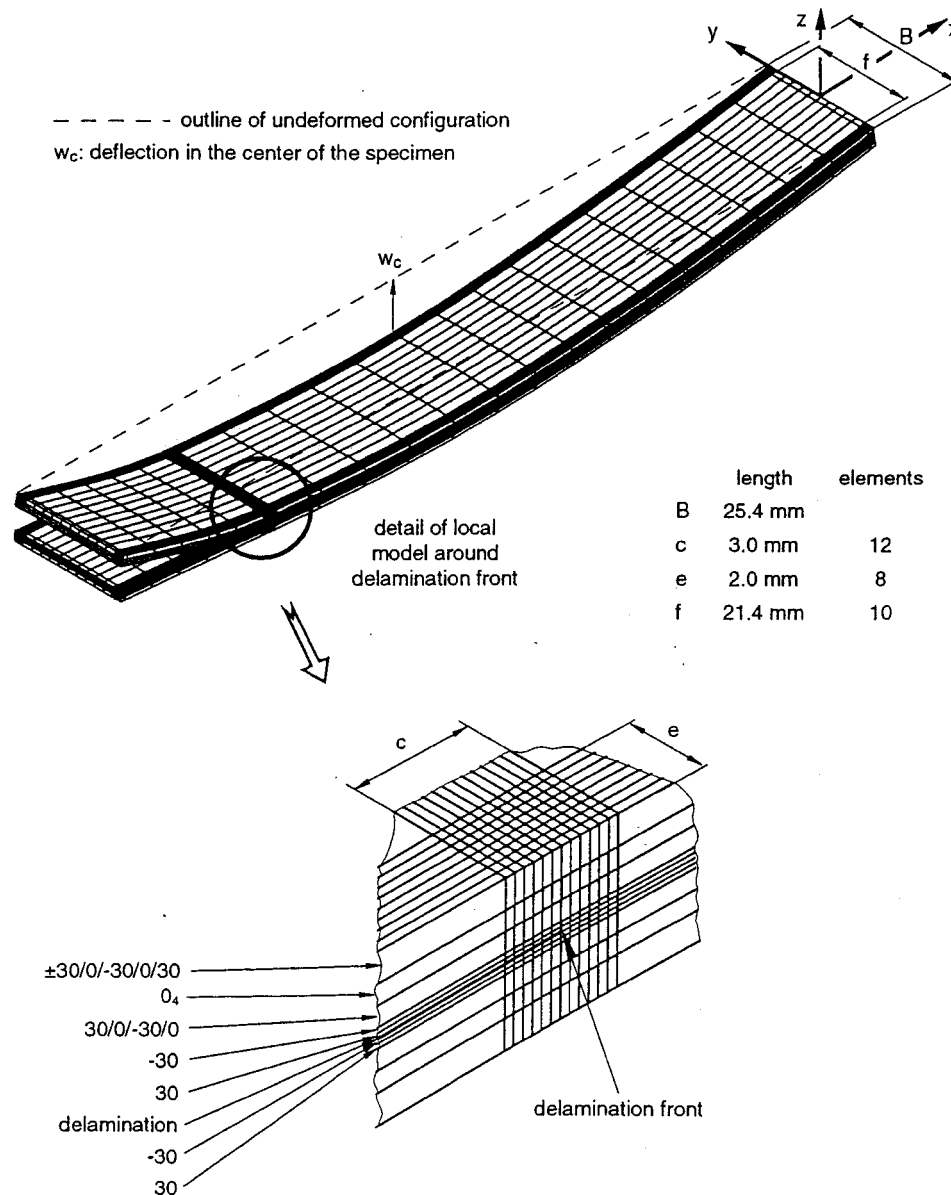|	length	elements
B	25.4 mm	
c	3.0 mm	12
e	2.0 mm	8
f	21.4 mm	10

Fig. 26   Three-dimensional finite element model of SLB specimen

Table 2. Mesh size at the crack tip for SLB specimen with multidirectional layup[a]

Length c of refined section (mm)	Number of elements n	Element length Δa (mm)	Relative element size $\Delta a/h$	Relative crack closure length $\Delta a/a$
3.0	3	1.0	7.874	0.029
3.0	6	0.5	3.937	0.014 5
3.0	12	0.25	1.968 5	0.007 3
3.0	24	0.125	0.984	0.003 65
3.0	48	0.062 5	0.492	0.001 83

[a]Layup $[\pm 30/0/-30/0/30/0_4/30/0/-30/0/-30/30/_\uparrow -30/30/30/0/30/0/-30/0_4/-30/0/30/0/\pm 30]$, C12K/ R6376 tape delamination length $a = 34.3$ mm, ply thickness $h = 0.127$ mm.

6 APPLICATION OF THE VIRTUAL CRACK CLOSURE TECHNIQUE TO ENGINEERING PROBLEMS

Selected engineering problems where the virtual crack closure technique is applied to fracture of composite structures are referenced in this section. Two examples from recent studies showing the application of VCCT to 2D and 3D finite element analyses are discussed in more detail.

6.1 Applying the virtual crack closure technique with two-dimensional finite element analysis

Two-dimensional finite element models where the crack or delamination is simulated as a line have been used exten-

sively in the past. In general 2D models are preferred by industry due to the fact that modeling time, as well as computational time, remains affordable, especially if many different configurations have to be analyzed during the initial design phase. However, the geometry, boundary conditions, and other properties across the entire width are inherently constant in a 2D finite element model. Additionally, a two-dimensional plane-stress model in the $x\text{-}y$ plane imposes the out of plane stresses to be zero ($\sigma_{zz} = \tau_{xz} = \tau_{yz} = 0$) and allows the displacement to be the free parameter. A plane-strain model in the $x\text{-}y$ plane, on the other hand, imposes the out of plane strains to be zero ($\varepsilon_{zz} = \gamma_{xz} = \gamma_{yz} = 0$), which excessively constrains the plies. The effect of 2D modeling

Fig. 27 Influence of the number of elements in refined section on computed mode I strain energy release rate distribution across the width of a SLB specimen

Fig. 29 Influence of the number of elements in refined section on computed mode III strain energy release rate distribution across the width of a SLB specimen
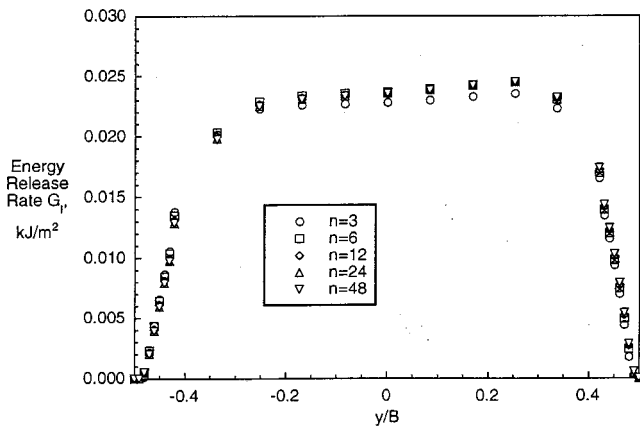

Fig. 28 Influence of the number of elements in refined section on computed mode II strain energy release rate distribution across the width of a SLB specimen
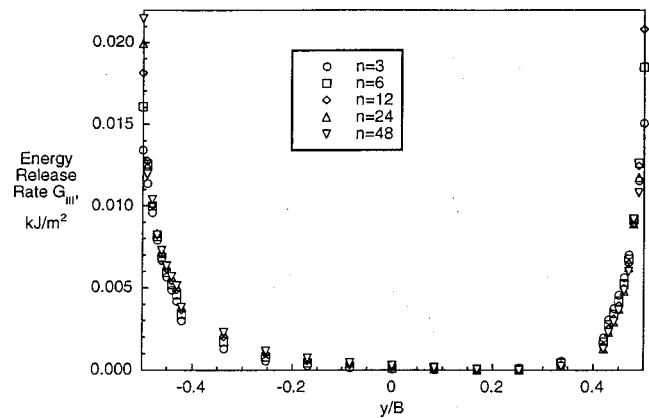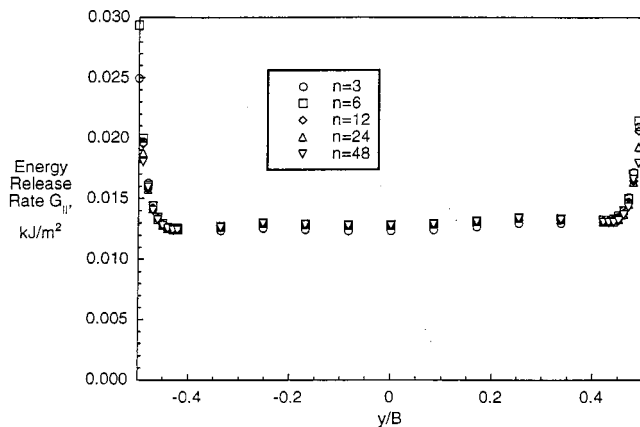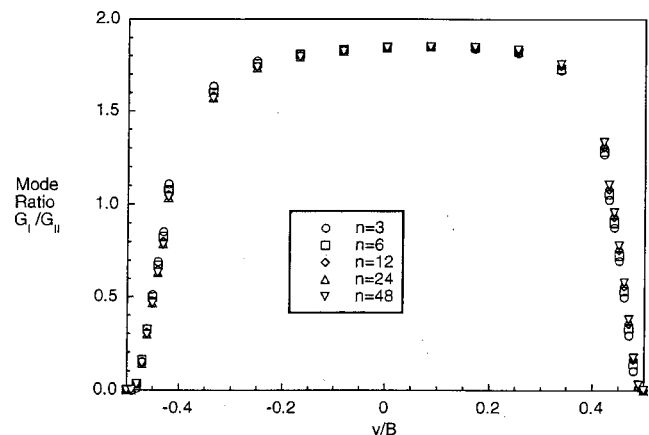

Fig. 30 Influence of the number of elements in refined section on mode ratio distribution across the width of a SLB specimen

assumptions is most marked for 45° plies because of their high in-plane Poisson's ratio, while it is small for 0° and 90°. The influence of 2D finite element modeling assumptions on computed energy release rates was studied in detail in Ref. [105]. Based on the results of this investigation it is recommended to use results from plane stress and plane strain models as upper and lower bounds. Two-dimensional models may also be used to qualitatively evaluate the variation of energy release rates and mixed-mode ratios with delamination length. For more accurate predictions, however, a 3D analysis is required.

Two-dimensional finite element models have been used to study the behavior of specimens used and suggested for fracture toughness testing in Refs. [106–114] and three-point bending specimen [115]. Iosipescu specimens were studied in Refs. [116], [117]. The behavior of edge delaminations was investigated in Refs. [5], [20], [118] and the failure of

composite hat stringer pull-of specimens was examined in Refs. [119], [120]. The failure of lap joints was investigated in Refs. [121], [122] and the durability of bonded joints in Ref. [123]. The virtual crack closure technique was also used to investigate the facesheet delaminating from the sandwich core [124–127] as well as delamination buckling [128,129]. Delamination initiation from ply drops in general was studied in Ref. [130] while the initiation specific to rotorcraft flexbeams was investigated in Refs. [131], [132].

To illustrate the application of VCCT to structural delamination, an example is taken from the study of skin/stringer debond failure as shown in Fig. 31 [133]. The specimens consisted of a tapered laminate, representing the stringer, bonded onto a skin as shown in Fig. 31(a). An IM7/8552 graphite/epoxy system was used for both the skin and flange. The skin was made of prepreg tape and had a nominal ply thickness of 0.142 mm and a [45/−45/0/−45/45/90/90/−45/

(a) Specimen configuration

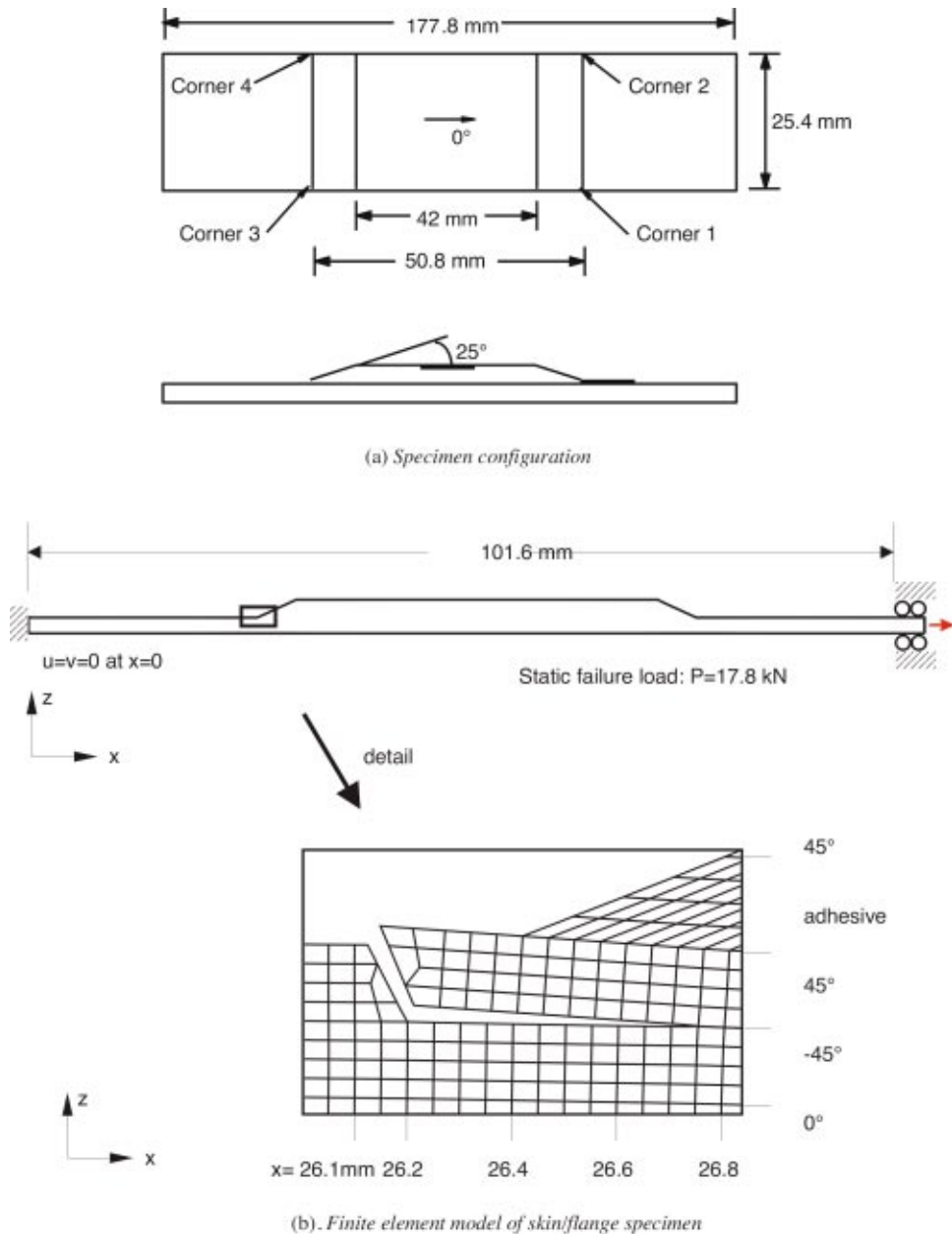(b). Finite element model of skin/flange specimen

Fig. 31 Skin/flange debonding specimen. a) Specimen configuration and b) finite element model of skin/flange specimen.

45/0/45/−45] layup. The flange was made of a plain-weave fabric of 0.208 mm nominal ply thickness. The flange layup was [45/0/45/0/45/0/45/0/45]$_f$, where the subscript f denotes fabric, 0 represents a 0°−90° fabric ply, and "45" represents a 0°−90° fabric ply rotated by 45°. Quasistatic tension tests were performed in a servohydraulic load frame where the specimens were mounted in hydraulic grips with a gage length of 101.6 mm as shown in Fig. 31(b). The value of the damage onset load, P, was averaged from four tests and determined to be 17.8 kN with a coefficient of variation of 8.9%. The tests were terminated when the flange debonded from the skin. Micrographic investigations showed that at corners 2 and 3, a delamination formed at the top 45°/−45° skin ply interface. The initial crack was modeled at the location suggested by the microscopic investigation as shown in the detail in Fig. 31(b). Finite element solutions were obtained using the commercial ABAQUS®/Standard finite element software. Eight-noded quadrilateral plane-stress (CPS8R) elements with quadratic shape functions and a reduced (2×2) integration scheme were utilized for the geometric nonlinear analyses. For this investigation, the delamination growing between the skin top 45° and −45° plies was extended by releasing multipoint constraints at the crack tip and in front of the crack tip. During a series of nonlinear finite element analyses, strain energy release rates were computed at each tip location for the loads applied in the experiments. A critical energy release rate G_c needs to be determined to predict delamination onset. This critical G is generally identified based on the shape of the total energy release rate versus delamination length curve, which is determined through analysis as shown in Fig. 32. The G_T versus x curve reached a maximum (as marked in Fig. 32) at some virtual delamination length and then decreased. The delamination was extended to a total simulated length of 2.2 mm to ascertain that the peak value had been captured. The total
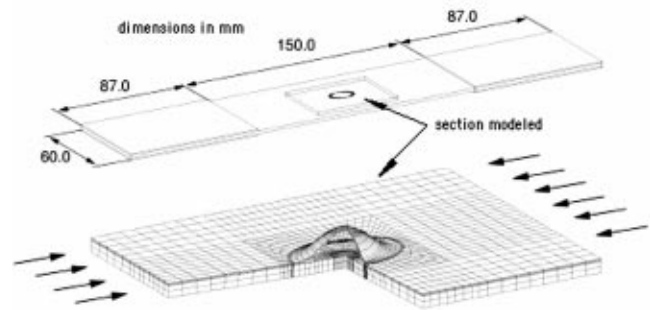
(a). Delamination buckling specimen and section modeled with three-dimensional solid elements
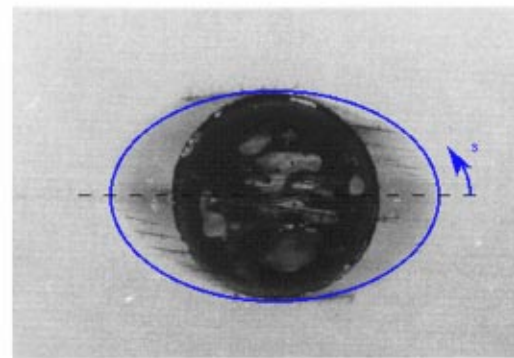
(b). X-Ray showing the initial circular delamination and detected growth after 200,000 load cycles

Fig. 34   Delamination buckling specimen. a) Delamination buckling specimen and section modeled with three-dimensional solid elements and b) x ray showing the initial circular delamination and detected growth after 200 000 load cycles.
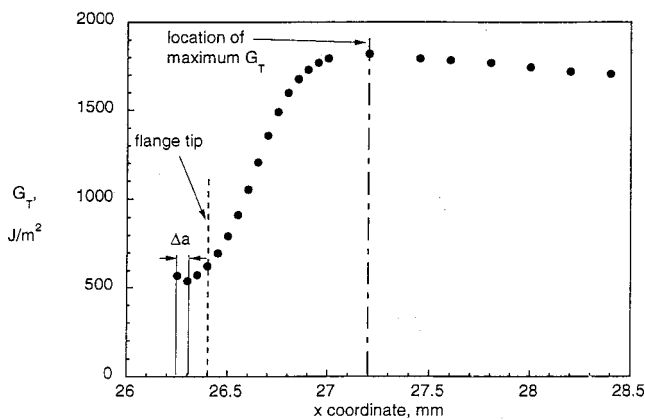

Fig. 32   Computed total strain energy release rate for delamination between top 45°/−45° skin plies
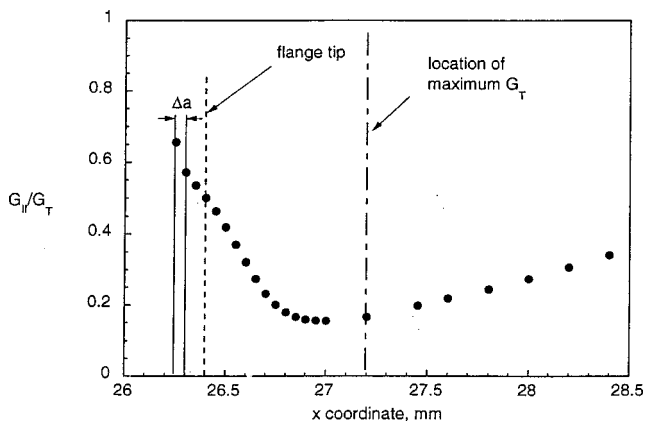

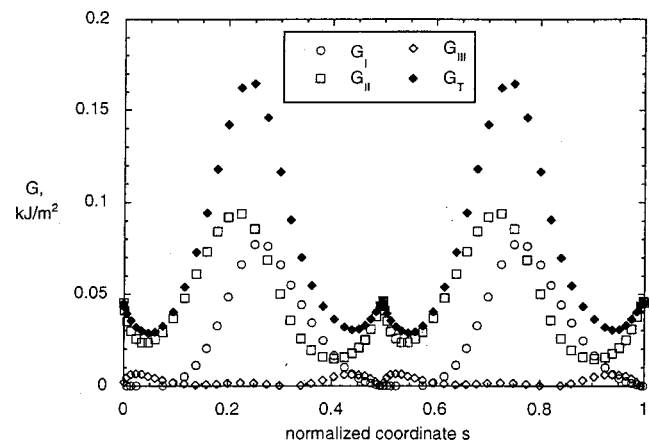Fig. 33   Computed mixed mode ratio for delamination between top 45°/−45° skin plies

Fig. 35   Computed mixed-mode energy release rate along detected delamination front after 200 000 load cycles

energy release rates and the corresponding mixed mode ratios G_{II}/G_T are plotted in Figs. 32 and 33. The maximum total energy release rate G_T as marked in the graph, was chosen as the critical value to be used for the fatigue life prediction [133]. This peak in G_T also corresponded to the maximum mode I percentage, ie, the minimum value of G_{II}/G_T in Fig. 33. Similar investigations of skin/flange debonding are reported in Refs. [134–137].

6.2 Applying the virtual crack closure technique to analysis with plate and shell elements

In a finite element model made of plate or shell type elements the delamination is represented as a two-dimensional discontinuity by two surfaces with identical nodal point coordinates. Flanagan developed a code based on sublaminate analysis and demonstrated its application to simple fracture toughness specimens, the curved-beam test and edge delamination [138]. The problem of a composite stringer separating from the skin has been investigated using plate and shell models in Refs. [74], [139], [140]. Fracture mechanics analyses performed by Glaessgen *et al* focused on the debonding

of stitched composite structures [141–143]. Delamination buckling has been investigated as well using plate/shell models [69,144–148].

6.3 Applying the virtual crack closure technique to analysis with solid finite elements

Three-dimensional finite element models have been used to study the behavior of specimens traditionally used in fracture toughness testing [18,23,27,67,77,78,98,100–102,149–153], three-point bending specimen [154] as well as the behavior of edge delaminations [155–157]. Skin-stiffener debonding was analyzed in Refs. [66], [105]. Damage in titanium-grahite hybrid lamiantes was investigated in Ref. [158] and Ireman *et al* studied the damage propagation in composite structural elements [159]. Three-dimensional models were also used to study the growth of near-surface delaminations in composite laminates under fatigue loading [81,160,161]. Delamination buckling has been investigated extensively using 3D models [69,79,130,162–172]. A comparison of 2D and 3D analysis for skin/stringer debond failure was performed in Refs. [173–175].

(a). *Intact region in front of the crack modeled with single nodes*

(b). *Intact region in front of the crack modeled with double nodes tied by multi-point contsraints*
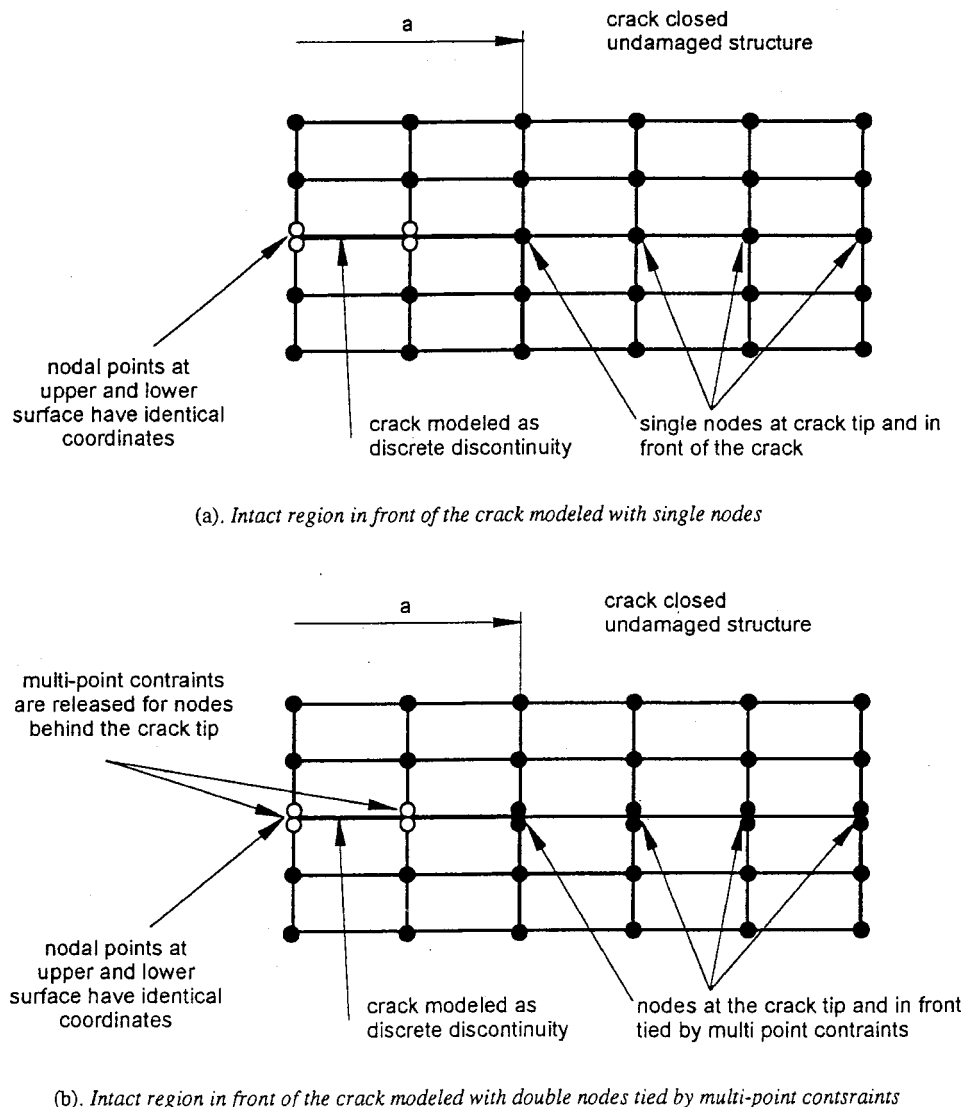
Fig. 36   Crack modeled as one-dimensional discontinuity. *a*) Intact region in front of the crack modeled with single nodes and *b*) intact region in front of the crack modeled with double nodes tied by multipoint constraints.

The example chosen is taken from an investigation of delamination buckling and growth as shown in Fig. 34(*a*) [81,160,176]. The specimens were made of T300/914C tape material with a $[\pm5/+45/\pm5/-45/0/\pm85/0/-45/\mp5/+45/\mp5]$ layup. An embedded circular delamination of 10 mm diameter at interface 2/3 was assumed to simulate an impact damage near the surface as shown in Fig. 34(*b*). The specimens were subjected to tension-compression ($R=-1$) fatigue loading. Stress maxima in the range of 220–240 N/mm^2 had shown to yield stable delamination growth. During the experiment, the out-of-plane (ie, buckling) deformation was monitored by the Moiré technique. Using numerical post-processing procedures, the size and shape of the delaminated sublaminate were determined from this information, yielding the delamination contours, which were used as input to the numerical model. Additional x-ray photographs [as shown in Fig. 34(*b*)] were used to verify this method. Finite element solutions were obtained using NOVA finite element software. Due to the extensive computation times seen for 3D models, a special layered element with eight nodes, formulated according to a continuum-based 3D shell theory, was used for the nonlinear simulations [177]. Interpenetration of the layers in the delaminated region was prevented by using a contact processor that utilizes a contractor target concept applying the penalty method [178]. Figure 34(*a*) shows the specimen outline, details of the section modeled and the deformed FE model. The distributions of the mixed-mode energy release rates along the front s_2 (ie, after 200 000 load cycles) as shown in Fig. 34(*b*), are plotted in Fig. 35. The global maximum of the total energy release rate G_T is now found perpendicular to the loading direction ($s\approx0.25$ and $s\approx0.75$) with a second maximum occurring in the loading direction. The values for interlaminar shear failure also reach their maximum perpendicular to the load direction ($s\approx0.22$ and $s\approx0.72$) and a second maximum for $s=0$ and $s=0.5$. This also holds for the G_I distribution where again the maximum is reached perpendicular to the loading direction; in loading direction, however, it decreases to zero. Details of the entire investigation are discussed in Ref. [179].

7   CONCLUDING REMARKS

The increased interest in using a fracture mechanics–based approach to assess the damage tolerance of composite structures in the design phase and during certification has renewed the interest in the virtual crack closure technique. Ef-
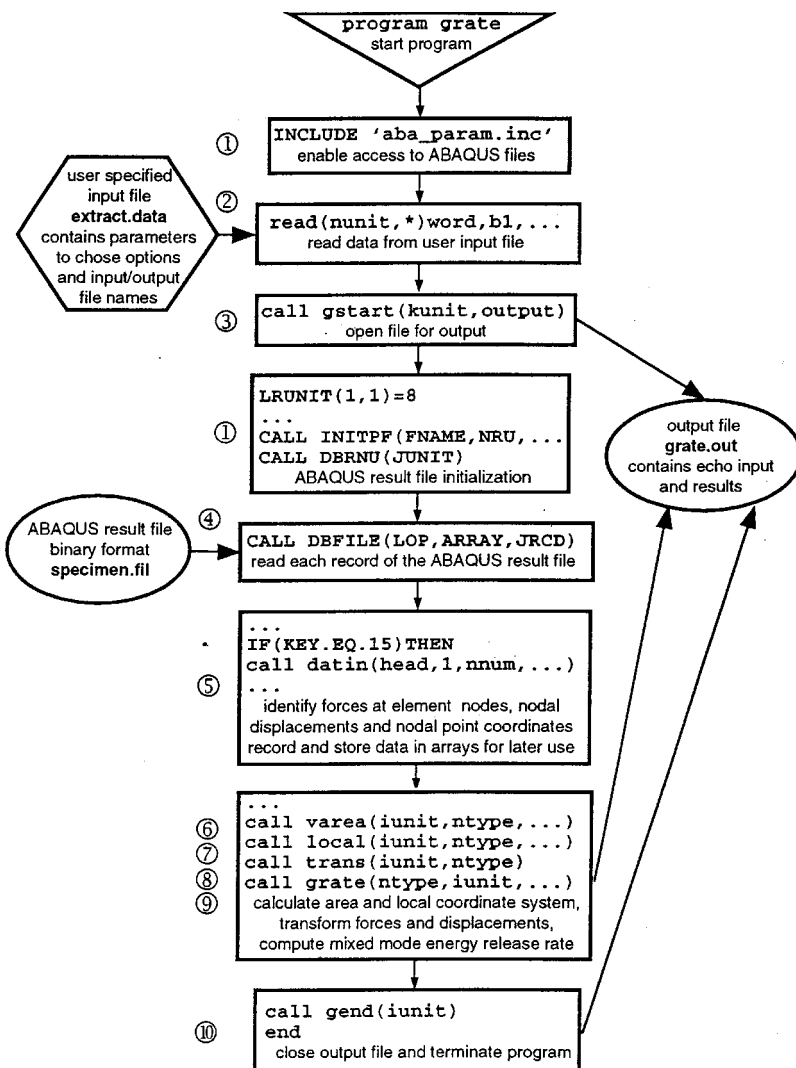

Fig. 37   Flow chart of routine extract.f to calculate strain energy release rates

forts are underway to incorporate these approaches in the *Composites Material MIL-17 Handbook*, which has been the motivation for the overview presented.

The approach used in the virtual crack closure technique was discussed. Equations for the use of the technique in conjunction with two-dimensional elements, three-element solids as well as plate/shell elements were given and insight into the application to engineering problems was provided. The paper, however, is not a comprehensive literature survey, but more a summary and review of issues relevant to the successful application of the virtual crack closure technique. Nevertheless, an effort was made to pay proper tribute to the relevant contributions made during a quarter century since the original publication.

ACKNOWLEDGMENTS

APPENDIX: IMPLEMENTATION OF THE VIRTUAL CRACK CLOSURE TECHNIQUE

Currently, the large commercial finite element codes do not offer the choice for calculating the mixed-mode energy release rates using the virtual crack closure technique (VCCT) as described in the main text. Therefore, the energy release rate components G_I, G_{II}, and G_{III} need to be computed by user-written subroutines. These subroutines may either interface directly with the finite element code during its execution, provided this option has been made available for this particular software, or operate as an entirely separate post-processing step. In both cases the strategy is similar and attention has to be given to the modeling of the discontinuity as shown in Fig. 36 and the calculation of the mixed-mode energy release rate as outlined in the flowchart of Fig. 37.

As mentioned in Sec. 3.1, the crack of length a in a two-dimensional finite element model is represented as a one-dimensional discontinuity by a line of nodes as shown in Figs. 5 and 36. Nodes at the top surface and the bottom surface have identical coordinates, however, are not connected with each other as shown in Fig. 36(*a*). The crack tip is represented by either a single node [Fig. 36(*a*)] or two nodes with identical coordinates coupled through multipoint constraints [Fig. 36(*b*)]. The undamaged section or the section where the crack is closed and the structure is still intact is modeled using single nodes [Fig. 36(*a*)] or two nodes with identical coordinates coupled through multipoint constraints [Fig. 36(*b*)]. It is generally up to the user to decide how to model the crack tip and the intact region. However, the use of multipoint constraints may be preferred if a crack propagation analysis is to be performed. The use of multipoint constraints may also be preferable if the finite element code

used provides *forces at constraints* as a standard output. This feature would render obsolete the step where element forces at nodes have to be retrieved and summed to obtain forces at the crack tip. The same logic applies to a finite element model made of plate/shell type elements or 3D solid elements, where the delamination of length a is represented as a 2D discontinuity by two surfaces.

The application of the virtual crack closure technique based on results from finite element analysis requires access to the element forces at nodes, the nodal point displacements and the nodal point coordinates. The flow chart, depicted in Fig. 37 as an example, shows an independent post-processing procedure where input data for the VCCT was extracted directly from an ABAQUS® binary result file. The strategy to use VCCT, however, is the same if data are retrieved from a data file in ASCII format or if a user-written subroutine interfaces directly with the finite element software during execution:

1) Establish interface with finite element sortware if required.

2) Provide input interface to read variable problem specific external data such as crack length, Young's modulus, etc, and control parameters such as element type, etc, which is generally not hard coded into the subroutine.

3) Create output file to store echo print of control parameters, input data, and retrieved data as well as intermediate and final results.

4) Read element forces, or forces at constraints, nodal point coordinates, and nodal displacements from binary result file, or output file in ASCII format or data bank if data are stored externally. Alternatively retrieve required data from specific common blocks or arrays of the finite element software if a user interface is provided.

5) Store the data retrieved in step (4) in external files, database, or internal common blocks and arrays for further access during the calculation.

6) Calculate area virtually closed, ΔA, using nodal point coordinates.

7) Calculate local coordinate system x', y', and z' at crack tip for geometrically nonlinear analysis and arbitrarily shaped delamination front as discussed in Secs. 3.3, 3.5, and 3.6.

8) *a*) Obtain the forces at the crack tip and in front of the crack tip from the forces at element nodes by summing the forces at common nodes from elements belonging either to the upper or the lower surface. This step may be skipped if forces at constraints are available directly from the finite element software.

    b) Obtain relative displacements between the surfaces from the nodal point displacements.

    c) Transform forces and displacements to local crack tip coordinate system.

9) Calculate mixed-mode strain energy release rates using the equations given for the individual element type and correct for different element lengths and widths if necessary.

10) Repeat steps (6) through (9) for all nodes along the delamination front and write results to output file.

REFERENCES

[1] Garg AC (1988), Delamination—A damage mode in composite structures, *Eng. Fract. Mech.* **29**(5), 557–584.

[2] Bolotin VV (1996), Delaminations in composite structures: its origin, buckling, growth and stability, *Composites, Part B* **27B**(2), 129–145.

[3] Pagano NJ and Schoeppner, GA (2000), Delamination of polymer matrix composites: Problems and assessment, *Comprehensive Composite Materials*, A Kelly and C Zweben (eds), Elsevier Science, Vol 2, 433–528.

[4] Tay TE (2003), Characterization and analysis of delamination fracture in composites: An overview of developments from 1990 to 2001, *Appl. Mech. Rev.* **56**(1), 1–32.

[5] O'Brien TK (1982), Characterization of delamination onset and growth in a composite laminate, pp. 140–167, *Damage in Composite Materials*, ASTM STP 775, Am Soc for Testing and Materials, Philadelphia, PA.

[6] O'Brien TK (1998), Interlaminar fracture toughness: The long and winding road to standardization, *Composites, Part B* **29**(1), 57–62.

[7] Martin RH (1998), Incorporating interlaminar fracture mechanics into design, pp. 83–92, *Int Conf on Designing Cost-Effective Composites*, IMechE Conference Transactions, London, U.K.

[8] O'Brien TK and Martin RH (1993), Round robin testing for mode I interlaminar fracture toughness of composite materials, *J. Compos. Technol. Res.* **15**, 269–281.

[9] O'Brien TK (1998), Composite interlaminar shear fracture toughness, G_{IIc}: Shear measurement or sheer Myth?, *Composite Materials: Fatigue and Fracture, Seventh Volume, ASTM STP 1330*, Am Soc for Testing and Materials, West Conshohocken, PA, 3–18.

[10] Reeder JR and Crews JH (1990), Mixed mode bending method for delamination testing, *AIAA J.* **28**, 1270–1276.

[11] Reeder JR and Crews JH (1992), Redesign of the mixed-mode bending delamination test to reduce nonlinear effects, *J. Compos. Technol. Res.* **14**(1), 12–19.

[12] Reeder JR (1993), A bilinear failure criterion for mixed-mode delamination, *Composite Materials: Testing and Design, Eleventh Volume, ASTM STP 1206*, Am Soc for Testing and Materials, Philadelphia, PA, 303–322.

[13] König M, Krüger, R, Kussmaul, K, v. Alberti, M, and Gädke, M (1997), Characterizing static and fatigue interlaminar fracture behavior of a first generation graphite/epoxy composite, *Composite Materials: Testing and Design, 13th Volume, ASTM STP 1242*, SJ Hooper (ed), Am Soc for Testing and Materials, Philadelphia, PA, 60–81.

[14] Hansen P and Martin R (1999), DCB, 4ENF and MMB delamination characterisation of S2/8552 and IM7/8552, N68171-98-M-5177, Materials Engineering Research Laboratory Ltd. (MERL), Hertford, UK.

[15] Lee SM (1990), Failure mechanics of edge delamination of composites, *J. Compos. Mater.* **24**, 1200–1212.

[16] Martin RH (1991), Evaluation of the split cantilever beam for mode III delamination testing, pp. 243–266, *Composite Materials: Fatigue and Fracture, Third Volume, ASTM STP 1110*, Philadelphia, PA.

[17] Robinson P and Song DQ (1994), Development of an improved mode III delamination test for composites, *Compos. Sci. Technol.* **52**(2), 217–233.

[18] Li J, Lee SM, Lee EW, and O'Brien TK (1997), Evaluation of the edge crack torsion ECT test for Mode III interlaminar fracture toughness of laminated composites, *J. Compos. Technol. Res.* **19**, 174–183.

[19] Rybicki EF and Kanninen MF (1977), A finite element calculation of stress intensity factors by a modified crack closure integral, *Eng. Fract. Mech.* **9**, 931–938.

[20] Rybicki EF, Schmueser DW, and Fox J (1977), An energy release rate approach for stable crack growth in the free-edge delamination problem, *J. Compos. Mater.* **11**, 470–487.

[21] Raju IS (1987), Calculation of strain-energy release rates with higher order and singular finite elements, *Eng. Fract. Mech.* **28**, 251–274.

[22] Buchholz FG, Grebner, H, Dreyer, KH, and Krome, H (1988), 2D- and 3D-applications of the improved and generalized modified crack closure integral method, *Computational Mechanics '88*, SN Atluri and G Yagawa (eds), Springer Verlag, New York.

[23] Miravete A and Jiménez MA (2002), Application of the finite element method to prediction of onset of delamination growth, *Appl. Mech. Rev.* **55**(2), 89–105.

[24] Ingraffea A and Wawrzynek, P (1995), FRANC2D: A case study in transfer of software technology, *Research Transformed into Practice:*

[25] Singh R, Carter BJ, Wawrzynek PA, and Ingraffea AR (1998), Universal crack closure integral for SIF estimation, *Eng. Fract. Mech.* **60**(2), 133–146.

[26] St. Doltsinis J, Knapp H, Streiner P, and Wüstenberg H, (1985), PERMAS-FM, Fracture mechanics, *User Manual*, Publication No 226, Rev C INTES GmbH, Stuttgart, Germany.

[27] Krüger R, König M, and Schneider T (1993), Computation of local energy release rates along straight and curved delamination fronts of unidirectionally laminated DCB- and ENF—specimens, *Proc of the 34th AIAA/ASME/ASCE/AHS/ASC SSDM Conf*, La Jolla, Am Inst of Aeronaut and Astronaut, Washington, 1332–1342.

[28] Hellen TK (1975), On the method of virtual crack extension, *Int. J. Numer. Methods Eng.* **9**, 187–207.

[29] Parks DM (1974), A stiffness derivative finite element technique for determination of crack tip stress intensity factors, *Int. J. Fract.* **10**, 487–502.

[30] Parks DM (1977), The virtual crack extension method for nonlinear material behavior, *Comput. Methods Appl. Mech. Eng.* **12**, 353–364.

[31] Parks DM (1978), Virtual crack extension: A general finite element technique for J-integral evaluation, *Numerical Methods in Fracture Mechanics*, AR Luxmoore and DRJ Owen (eds), Pineridge Press, Swansea, UK, 464–479.

[32] Delorenzi HG (1982), On the energy release rate and the J-integral for 3-D crack configurations, *Int. J. Fract.* **19**, 183–193.

[33] Delorenzi HG and Shih CD (1983), 3-D Elastic-plastic investigation of fracture parameters in side-grooved compact specimen, *Int. J. Fract.* **21**, 195–220.

[34] Delorenzi HG (1985), Energy release rate calculations by the finite element method, *Eng. Fract. Mech.* **21**, 129–143.

[35] Lin SC and Abel JF (1988), Variational aproach for a new direct-integration form of the virtual crack extension method, *Int. J. Fract.* **38**, 217–235.

[36] Claydon PW (1992), Maximum energy release rate distribution from a generalized 3D virtual crack extension method, *Eng. Fract. Mech.* **42**(6), 961–969.

[37] Hwang CG, Wawrzynek PA, Tayebi AK, and Ingraffea AR (1998), On the virtual crack extension method for calculation of the rates of energy release rate, *Eng. Fract. Mech.* **59**(4), 521–542.

[38] Ishikawa H (1980), A finite element analysis of stress intensity factors for combined tensile and shear loading by only a virtual crack extension, *Int. J. Fract.* **16**, R243–R246.

[39] Sha GT (1984), On the virtual crack extension technique for stress intensity factors and energy release rate calculations for mixed fracture mode, *Int. J. Fract.* **25**, R33–R42.

[40] Li FZ, Shih CF, and Needleman A (1985), A comparison of methods for calculating energy-release rates, *Eng. Fract. Mech.* **21**(2), 405–421.

[41] Moran B and Shih CF (1987), Crack tip and associated domain integrals from momentum and energy-balance, *Eng. Fract. Mech.* **27**(6), 615–642.

[42] Nikishkov GP and Atluri SN (1987), Calculation of fracture-mechanics parameters for an arbitrary 3-dimensional crack, by the equivalent domain integral method, *Int. J. Numer. Methods Eng.* **24**(9), 1801–1821.

[43] Nikishkov GP and Atluri SN (1987), An equivalent domain integral method for computing crack-tip integral parameters in nonelastic, thermomechanical fracture, *Eng. Fract. Mech.* **26**(6), 851–867.

[44] Raju IS and Shivakumar KN (1990), An equivalent domain integral method in the two-dimensional analysis mixed-mode crack problems, *Eng. Fract. Mech.* **37**(4), 707–725.

[45] Shivakumar KN and Raju IS (1992), An equivalent domain integral method for three-dimensional mixed-mode fracture problems, *Eng. Fract. Mech.* **42**(6), 935–959.

[46] Banks-Sills L (1991), Application of the finite element method to linear elastic fracture mechanics, *Appl. Mech. Rev.* **44**(10), 447–461.

[47] Chow WT and Atluri SN (1997), Stress intensity factors as the fracture parameters for delamination crack growth in composite laminates, *Composites, Part B* **28B**(4), 375–384.

[48] Gosz M and Moran B (2002), An interaction energy integral method for computation of mixed-mode stress intensity factors along non-planar crack fronts in three dimensions, *Eng. Fract. Mech.* **69**(3), 299–319.

[49] Park O and Sankar BV (2002), Crack-tip force method for computing energy release rate in delaminated plates, *Compos. Struct.* **55**(4), 429–434.

[50] Schön J and Andersson B (1998), Calculation of mode-separated energy release rates during delamination growth, *Proc of Am Soc for*

Composites—13th Technical Conf on Composite Materials, Am Soc for Composites Dayton, OH.

[51] Mukhopadhyay NK, Kakodkar A, and Maiti SK (1998), Further considerations in modified crack closure integral based computation of stress intensity factor in BEM, *Eng. Fract. Mech.* **59**(3), 269–279.

[52] Irwin GR (1958), Fracture I, *Handbuch der Physik VI*, Flügge (ed), Springer Verlag, Berlin, Germany, 558–590.

[53] Broek D (1991), *Elementary Engineering Fracture Mechanics*, 4th Revised Edition, Kluwer Academic Publishers, Dordrecht, Netherlands.

[54] Buchholz FG (1984), Improved formulae for the FE-calculation of the strain energy release rate by the modified crack closure integral method, *Proceedings of the 4th World Congress on Finite Elements*, Interlaken, Robinson and Assoc, Dorset, 650–659.

[55] Buchholz FG and Meiners B (1984), On the accuracy of the modified crack closure integral method in combination with higher order finite elements, *Accuracy Estimates and Adaptive Refinements in Finite Element Computations*, *Proc of Int Conf*, Lisbon, Technical University of Lisbon, Lisbon, **I**, 131–140.

[56] Barsoum RS (1976), On the use of isoparametric finite elements in linear fracture mechanics, *Int. J. Numer. Methods Eng.* **10**, 25–37.

[57] Barsoum RS (1977), Triangular quarter-point elements as elastic and perfectly-plastic crack tip elements, *Int. J. Numer. Methods Eng.* **11**, 85–98.

[58] Murti V and Valliappan S (1986), A universal optimum quarter point element, *Eng. Fract. Mech.* **25**(2), 237–258.

[59] Narayana KB, Dattaguru B, Ramamurthy TS, and Vijayakumar K (1990), Modified crack closure integral using six-noded isoparametric quadrilateral singular elements, *Eng. Fract. Mech.* **36**(6), 945–955.

[60] Henshell RD and Shaw KG (1975), Crack tip finite elements are unnecessary, *Int. J. Numer. Methods Eng.* **9**, 496–507.

[61] Ramamurthy TS, Krishnamurthy T, Narayana KB, Vijayakumar K, and Dattaguru B (1986), Modified crack closure integral method with quarter point elements, *Mech. Res. Commun.* **13**(4), 179–186.

[62] Lim IL, Johnston IW, and Choi SK (1991), The use of transition-elements, *Eng. Fract. Mech.* **40**(6), 975–983.

[63] Narayana KB and Dattaguru B (1996), Certain aspects related to computation by modified crack closure integral (MCCI), *Eng. Fract. Mech.* **55**(2), 335–339.

[64] Sethuraman R and Maiti SK (1988), Finite element based computation of strain energy release rate by modified crack closure integral, *Eng. Fract. Mech.* **30**(2), 227–231.

[65] Shivakumar KN, Tan PW, and Newman JC (1988), A virtual crack-closure technique for calculating stress intensity factors for cracked three dimensional bodies, *Int. J. Fract.* **36**, R43–R50.

[66] Raju IS, Sistla R, and Krishnamurthy T (1996), Fracture mechanics analyses for skin-stiffener debonding, *Eng. Fract. Mech.* **54**(3), 371–385.

[67] Raju IS, Shivakumar KN, and Crews JH, Jr (1988), Three-dimensional elastic analysis of a composite double cantilever beam specimen, *AIAA J.* **26**, 1493–1498.

[68] Roeck GD and Wahab MMA (1995), Strain energy release rate formulae for 3D finite element, *Eng. Fract. Mech.* **50**, 569–580.

[69] Whitcomb JD and Shivakumar KN (1989), Strain-energy release rate analysis of plates with postbuckled delaminations, *J. Compos. Mater.* **23**, 714–734.

[70] Buchholz FG (1994), Finite element analysis of a 3D mixed-mode fracture problem by virtual crack closure integral method, *Proceedings of the Indo-German Workshop*, AVK Murthy and FG Buchholz (eds), Indian Institute of Science, Interline Publications, Bangalore, 7–12.

[71] Narayana KB, George S, Dattaguru B, Ramamurthy TS, and Vijayakumar K (1994), Modified crack closure integral (MCCI) for 3-d problems using 20-noded brick elements, *Fatigue Fract. Eng. Mater. Struct.* **17**(2), 145–157.

[72] Singh R, Patel SK, and Dattaguru B (1999), Decomposed crack closure integrals for estimation of SIF variations, *Eng. Fract. Mech.* **63**(2), 165–178.

[73] He W-J, Lin Y, and Ding H-J (1997), A three-dimensional formula for determining stress intensity factors in finite element analysis of cracked bodies, *Eng. Fract. Mech.* **57**(4), 409–415.

[74] Wang JT and Raju IS (1996), Strain energy release rate formulae for skin-stiffener debond modeled with plate elements, *Eng. Fract. Mech.* **54**(2), 211–228.

[75] Glaessgen EH, Riddell WT, and Raju IS (1998), Effect of shear deformation and continuity on delamination modeling with plate elements, *39rd AIAA/ASME/ASCE/AHS/ASC Structures, Structural Dynamics and Materials Conference*.

[76] Glaessgen EH, Riddell WT, and Raju IS (2002), Nodal constraint,

[77] König M, Krüger R, and Rinderknecht S (2000), Finite element analysis of delamination growth in a multidirectional composite ENF specimen, 345–365, *Composite Materials: Theory and Practice*, P Grant and CQ Rousseau (eds), ASTM STP 1383. Am Soc for Testing and Materials, West Conshohocken, PA.

[78] Krueger R and O'Brien TK (2001), A shell/3D modeling technique for the analysis of delaminated composite laminates, *Composites, Part A* **32**(1), 25–44.

[79] Whitcomb JD (1990), Mechanics of instability-related delamination growth, *Composite Materials: Testing and Design, Ninth Volume*, SP Garbo (ed), ASTM STP 1059, Am Soc for Testing and Materials, Philadelphia, PA, 215–230.

[80] Smith SA and Raju IS (1998), Evaluation of stress-intensity factors using general finite-element models, *Fatigue and Fracture Mechanics, 29th Volume, ASTM STP 1321*, TL Panontin and SD Sheppard (eds), Am Soc for Testing and Materials, West Conshohocken, PA.

[81] Krüger R and König M (1997), Prediction of delamination growth under cyclic loading, *Composite Materials: Fatigue and Fracture, Sixth Volume, ASTM STP 1285*, EA Armanios (ed), Am Soc for Testing and Materials, West Conshohocken, PA, 162–178.

[82] Ferrie CH and Rousseau CQ (2001), A method of applying VCCT to corner crack nodes, *Proc of Am Soc for Composites*, *16th Annual Technical Conference on Composite Materials*, Blacksburg, VA, Am Soc for Composites, Dayton, OH.

[83] Raju IS, Crews JH, and Aminpour MA (1988), Convergence of strain energy release rate components for edge-delaminated composite laminates, *Eng. Fract. Mech.* **30**(3), 383–396.

[84] Hwu C and Hu J (1992), Stress intensity factors and energy release rates of delaminations in composite laminates, *Eng. Fract. Mech.* **42**(6), 977–988.

[85] Sun CT and Jih CJ (1987), On strain energy release rates for interfacial cracks in bimaterial media, *Eng. Fract. Mech.* **28**(1), 13–20.

[86] Sun CT and Manoharan MG (1989), Strain energy release rates of an interfacial crack between two orthotropic solids, *J. Compos. Mater.* **23**, 460–478.

[87] Dattaguru B, Venkatesha KS, Ramamurthy TS, and Buchholz FG (1994), Finite element estimates of strain energy release rate components at the tip of an interface crack under mode I loading, *Eng. Fract. Mech.* **49**(3), 451–463.

[88] Beuth JL and Narayan SH (1997), Separation of crack extension modes in composite delamination problems, *Composite Materials: Fatigue and Fracture, Sixth Volume, ASTM STP 1285*, EA Armanios (ed), Am Soc for Testing and Materials, West Conshohocken, PA, 324–342.

[89] Huang H and Kardomateas GA (2001), Mixed-mode stress intensity factors for cracks located at or parallel to the interface in bimaterial half planes, *Int. J. Solids Struct.* **38**(21), 3719–3734.

[90] Qian W and Sun CT (1997), Calculation of stress intensity factors for interlaminar cracks in composite laminates, *Compos. Sci. Technol.* **57**(6), 637–650.

[91] Qian W and Sun CT (1998), Methods for calculating stress intensity factors for interfacial cracks between two orthotropic solids, *Int. J. Solids Struct.* **35**(25), 3317–3330.

[92] Boniface V and Simha KRY (1999), Re-examination of crack opening model of interface fracture, *Eng. Fract. Mech.* **64**(6), 677–691.

[93] Sun CT and Qian W (1997), The use of finite extension strain energy release rates in fracture of interfacial cracks, *Int. J. Solids Struct.* **34**(20), 2595–2609.

[94] Venkatesha KS, Dattaguru B, and Ramamurthy TS (1996), Finite-element analysis of an interface crack with large crack-tip contact zones, *Eng. Fract. Mech.* **54**(6), 847–860.

[95] Venkatesha KS, Dattaguru B, and Ramamurthy TS (1996), Generalized modified crack closure integral (GMCCI) and its application to interface crack problems, *Comput. Struct.* **60**(4), 665–676.

[96] Venkatesha KS, Ramamurthy TS, and Dattaguru B (1998), A study of the behavior of subinterface cracks in bimaterial plates, *Eng. Fract. Mech.* **59**(2), 241–252.

[97] Zou Z, Reid SR, Soden PD, and Li S (2001), Mode separation of energy release rate for delamination in composite laminates using sublaminates, *Int. J. Solids Struct.* **38**(15), 2597–2613.

[98] Morais ABd, Moura MFd, Marques AT, and Castro PTd (2002), Mode-I interlaminar fracture of carbon/epoxy cross-ply composites, *Compos. Sci. Technol.* **62**(5), 679–686.

[99] O'Brien TK (2001), personal communication.

[100] Krüger R (1994), Three dimensional finite element analysis of multi-directional composite DCB, SLB and ENF specimens ISD-Report

No 94/2, Institute for Statics and Dynamics of Aerospace Structures, University of Stuttgart.

[101] Davidson BD, Krüger R, and König M(1995), Three dimensional analysis and resulting design recommendations for unidirectional and multidirectional end-notched flexure tests, *J. Compos. Mater.* **29**(16), 2108–2133.

[102] Davidson BD, Krüger R, and König M(1995), Three dimensional analysis of center delaminated unidirectional and multidirectional single leg bending specimens, *Compos. Sci. Technol.* **54**(4), 385–394.

[103] Krueger R and O'Brien TK (2000), A shell/3D modeling technique for the analysis of delaminated composite laminates, NASA/TM-2000-210287, ARL-TR-2207.

[104] Sih GC, Paris PC, and Irwin GR(1965), On cracks in rectilinearly anisotropic bodies, *Int. J. Fract. Mech.* **1**, 189–203.

[105] Krueger R, Paris IL, O'Brien TK, and Minguet PJ(2002), Comparison of 2D finite element modeling assumptions with results from 3D analysis for composite skin-stiffener debonding, *Compos. Struct.* **57**(1–4), 161–168.

[106] Ramakumar RL and Whitcomb JD (1985), Characterization of mode I and mixed-mode delamination growth in T300/5208 graphite/epoxy, *Delamination and Debonding of Materials, ASTM STP 876*, WS Johnson (ed), Am Soc for Testing and Materials, Philadelphia, PA, 315–335.

[107] Rybicki EF, Hernandez TD, Deibler JE, Knight RC, and Vinson SS (1987), Mode I and mixed mode energy release rate values for delamination of graphite/epoxy test specimens, *J. Compos. Mater.* **21**, 105–123.

[108] Tanzawa Y, Watanabe N, and Ishikawa T(2001), FEM simulation of a modified DCB test for 3-D orthogonal interlocked fabric composites, *Compos. Sci. Technol.* **61**(8), 1097–1107.

[109] Rhee KY (1997), On the validity of applying the elastic work factor approach to determine G_{Ic} of fiber-reinforced laminated composites, *Compos. Struct.* **37**(1), 57–63.

[110] Rikards R, Buchholz FG, Wang H, Bledzki AK, Korjakin A, and Richard HA(1998), Investigation of mixed mode I/II interlaminar fracture toughness of laminated composites by using a CTS type specimen, *Eng. Fract. Mech.* **61**(3–4), 325–342.

[111] Rikards R, Korjakin A, Buchholz FG, Wang H, Bledzki AK, and Wacker G(1998), Interlaminar fracture toughness of GFRP influenced by fiber surface treatment, *J. Compos. Mater.* **32**(17), 1528–1559.

[112] Jose S, Kumar RR, Janab MK, and Rao GV(2001), Intralaminar fracture toughness of a cross-ply laminate and its constituent sub-laminates, *Compos. Sci. Technol.* **61**, 1115–1122.

[113] Pieracci A, Davidson BD, and Sundararaman V(1998), Nonlinear analyses of homogeneous, symmetrically delaminated single leg bending specimens, *J. Compos. Technol. Res.* **20**(3), 170–178.

[114] Schuecker C and Davidson BD (2000), Effect of friction on the perceived mode II delamination toughness from three- and four-point bend end-notched flexure tests, *Composite Materials: Theory and Practice, ASTM STP 1383*, P Grant and CQ Rousseau (eds) Am Soc for Testing and Materials, West Conshohocken, PA, 334–344.

[115] Wang H, Ding, S, Buchholz, FG, and Rikards, R (1994), Delamination analysis for 2D- and 3D-models of a cross-ply laminated three-point bending specimen, *Localized Damage III*, MH Alíabadí, A Carpinterí, S Kalinsky, and DJ Cartwright (eds), Computational Mechanics Publ, Southampton, UK and Boston, MA, 251–258.

[116] Bansal A and Kumosa M(1998), Analysis of double edge-cracked iosipescu specimens under biaxial loads, *Eng. Fract. Mech.* **59**(1), 89–100.

[117] Buchholz FG, Bürger M, Kumosa M, and Eggers H (1990), Mixed-mode fracture analysis of orthotropic laminates by local and global energy methods, *Numerical Methods in Fracture Mechanics*, AR Luxmorre and DRJ Owen (eds), Pineridge Press, Swansea, UK, 391–402.

[118] Whitcomb JD and Raju IS (1985), Analysis of interlaminar stresses in thick composite laminates with and without edge delamination, *Delamination and Debonding of Materials, ASTM STP 876*, WS Johnson (ed), Am Soc for Testing and Materials, Philadelphia, PA, 69–94.

[119] Li J, O'Brien TK, and Rousseau CQ(1997), Test and analysis of composite hat stringer pull-off test specimens, *J. Am. Helicopter Soc.* 350–357.

[120] Li J (2000), Flange delamination prediction in composite structures with ply waviness, *AIAA J.* **38**(5), 893–897.

[121] Wahab MMA (2000), On the use of fracture mechanics in designing a single lap adhesive joint, *J. Adhes. Sci. Technol.* **14**(6), 851–865.

[122] Qin M and Dzenis Y (2001), Nonlinear numerical and experimental analysis of single lap adhesive composie joints with delaminated ad-

herends, *Proc of Thirteenth Int Conf on Composite Materials (ICCM13)*, Y Zhang (ed), Beijing.

[123] Johnson WS, Butkus, LM, and Valentin, RV (1998), Applications of fracture mechanics to the durability of bonded composite joints, DOT/FAA/AR-97/56, US Department of Transportation, Federal Aviation Administration.

[124] Goswamia S and Becker W(2001), The effect of facesheet/core delamination in sandwich structures under transverse loading, *Compos. Struct.* **54**(4), 515–521.

[125] Ratcliffe JGA (2001), Ph.D. thesis, The University of Liverpool.

[126] Cantwell WJ, Scudamore R, Ratcliffe J, and Davies P(1999), Interfacial fracture in sandwich laminates, *Compos. Sci. Technol.* **59**, 2079–2085.

[127] Glaessgen EH, Sleight DW, Krishnamurthy T, and Raju IS (2001), Analyses for debonding of stitched composite sandwich structures using improved constitutive models, *42nd AIAA/ASME/ASCE/AHS/ASC Structures, Structural Dynamics, and Materials Conference.*

[128] Whitcomb JD (1984), Strain-energy release rate analysis of cyclic delamination growth in compressively loaded laminates, *Effect of Defects in Composite Materials, ASTM STP 836*, Am Soc for Testing and Materials, Philadelphia, PA, 175–193.

[129] Hwang S-F and Mao C-P(2001), Failure of delaminated interply hybrid composite plates under compression, *Compos. Sci. Technol.* **61**(11), 1513–1527.

[130] Singh KL, Dattaguru B, Ramamurthy TS, and Mangalgiri PD (1999), 3D fracture analysis of delaminations in laminated composites, *Modeling and Simulation Based Engineering*, Vol II, SN Atluri and PE O'Donoghue (eds), Tech Science Press, Encino, CA, 1592–1597.

[131] Murri GB, O'Brien TK, and Rousseau CQ(1998), Fatigue life methodology for tapered composite flexbeam laminates, *J. Am. Helicopter Soc.* **43**, 146–155.

[132] Murri GB, Schaff JR, and Dobyns AL (2001), Fatigue and damage tolerance analysis of a hybrid composite tapered flexbeam, *Proceedings of the American Helicopter Society 57th Annual Forum*, Washington, DC, May 9–11.

[133] Krueger R, Paris IL, O'Brien TK, and Minguet PJ(2002), Fatigue life methodology for bonded composite skin/stringer configurations, *J. Compos. Technol. Res.* **24**(2), 56–79.

[134] Minguet PJ and O'Brien, TK (1995), Analysis of composite skin/stringer bond failures using a strain energy release rate approach, *The Tenth International Conference on Composite Materials*, Vol I, A Poursartip and K Street (eds), 245–252.

[135] Minguet PJ (1997), Analysis of the strength of the interface between frame and skin in a bonded composite fuselage panel, *The 38rd AIAA/ASME/ASCE/AHS/ASC Structures, Structural Dynamics and Materials Conference*, 2783–2790.

[136] Krueger R, Cvitkovich MK, O'Brien TK, and Minguet PJ(2000), Testing and analysis of composite skin/stringer debonding under multi-axial loading, *J. Compos. Mater.* **34**(15), 1263–1300.

[137] Hoyt DM, Ward SH, and Minguet PJ(2002), Strength and fatigue life modeling of bonded joints in composite structure, *J. Compos. Technol. Res.* **24**(3), 190–210.

[138] Flanagan G (1994), A general sublaminate analysis method for determining strain energy release rates in composites, *The 35rd AIAA/ASME/ASCE/AHS/ASC Structures, Structural Dynamics and Materials Conference*, 381–389.

[139] Yap JWH, Scott ML, Thomson RS, and Hachenberg D(2002), The analysis of skin-to-stiffener debonding in composite aerospace structures, *Compos. Struct.* **57**(1–4), 425–435.

[140] Kumar RR and Rao GV (2001), Some studies on interlaminar and intralaminar fracture toughness of multilayered composite structures, *Proceedings of the Thirteenth International Conference on Composite Materials (ICCM13)*, Y Zhang (ed), Beijing.

[141] Glaessgen EH, Raju IS, and Poe CC (1998), Fracture mechanics analysis of stitched stiffener-skin debonding, *The 39th AIAA/ASME/ASCE/AHS/ASC Structures, Structural Dynamics and Materials Conference*, Long Beach, California, AIAA 98-2022, April 20–23.

[142] Glaessgen EH, Raju, IS, and Poe CC (1999), Delamination and stitch failure in stitched composite joints, *Proceedings of the 40th AIAA/ASME/ASCE/AHS/ASC Structures, Structural Dynamics and Materials Conference.*

[143] Glaessgen EH, Raju IS, and Poe CC (1999), Debonding of stitched composite joints: Testing and analysis, *Society for Experimental Mechanics Spring Conference and Exposition*, Cincinnati, Ohio, June 7–9.

[144] Rinderknecht S and Kröplin B (1995), A finite element model for the delamination in composite plates, *Mech. Compos. Mater. Struct.* **2**, 19–47.

[145] Rinderknecht S and Kroplin B(1997), Computational method for the

analysis of delamination growth in composite plates, *Comput. Struct.* **64**(1–4), 359–374.

[146] Klug J, Wu XX, and Sun CT(1996), Efficient modeling of postbuckling delamination growth in composite laminates using plate elements, *AIAA J.* **34**(1), 178–184.

[147] Zheng S and Sun CT(1998), Delamination interaction in laminated structures, *Eng. Fract. Mech.* **59**(2), 225–240.

[148] Reeder J, Song K, Chunchu P, and Ambur D (2002), Postbuckling and growth of delaminations in composite plates subjected to axial compression, *The 43rd AIAA/ASME/ASCE/AHS/ASC Structures, Structural Dynamics, and Materials Conference*.

[149] Crews JH, Shivakumar KN, and Raju IS(1991), Strain energy release rate distribution for double cantilever beam specimens, *AIAA J.* **29**, 1686–1691.

[150] Davidson BD, Krüger R, and König M(1996), Effect of stacking sequence on energy release rate distributions in multidirectional DCB and ENF specimens, *Eng. Fract. Mech.* **55**(4), 557–569.

[151] Shivakumar K, Ghantae S, and Sharpe M (2001), Split angle-ply beam specimen for measurement of fracture toughness with mode III stress state, *Proc of the Thirteenth Int Conf on Composite Materials (ICCM13)*, Y Zhang (ed), Beijing.

[152] Suemasu H (1999), An experimental method to measure the mode-III interlaminar fracture toughness of composite laminates, *Compos. Sci. Technol.* **59**(7), 1015–1021.

[153] Dhondt G, Chergui A, and Buchholz F-G(2001), Computational fracture analysis of different specimens regarding 3D and mode coupling effects, *Eng. Fract. Mech.* **68**(4), 383–401.

[154] Wang H, Buchholz FG, and Rikards R (1995), Delamination analysis of an angle-ply laminated three-point bending specimen, *Computational Mechanics '95: Theory and Application*, SN Atluri, G Yagawa, and TA Cruse (eds), Springer, Heidelberg, Vol. II, 2323–2328.

[155] Salpekar SA and O'Brien TK (1991), Combined effect of matrix cracking and free edge on delamination, *Composite Materials: Fatigue and Fracture, Third Volume, ASTM STP 1110*, Am Soc for Testing and Materials, Philadelphia, PA, 287–311.

[156] Kaczmarek K, Wisnom MR, and Jones MI(1998), Edge delamination in curved $(0_4/\pm45_6)_s$ glass-fibre/epoxy beams loaded in bending, *Compos. Sci. Technol.* **58**(1), 155–161.

[157] Lindemann J and Becker W(2002), The tendency for free-edge delamination in laminates and its minimization, *Compos. Sci. Technol.* **62**(2), 233–242.

[158] Burianek DA and Spearing SM (2001), Interacting damage modes in titanium-graphite hybrid laminates, *Proc of the Thirteenth Int Conf on Composite Materials (ICCM13)*, Y Zhang (ed), Beijing.

[159] Ireman T, Thesken JC, Greenhalgh E, Sharp R, Gädke M, Maison S, Ousset Y, Roudolff F, and Barbera AL(1996), Damage propagation in composite structural elements-coupon experiments and analyses, *Compos. Struct.* **36**(3–4), 209–220.

[160] Krüger R, König M, and Kröplin B (1997), Delamination growth in CFRP-laminates: development of a predictive tool based on computational fracture mechanics, *Proc of the 38th AIAA/ASME/ASCE/AHS/ASC SSDM Conf*, Kissimmee, FL, Am Institute of Aeronautics and Astronautics, Reston, VA, 2064–2072.

[161] Pradhan SC and Tay TE(1998), Three-dimensional finite element modeling of delamination growth in notched composite laminates under compression loading, *Eng. Fract. Mech.* **60**(2), 157–171.

[162] Whitcomb JD (1989), Three-dimensional analysis of a postbuckled embedded delamination, *J. Compos. Mater.* **23**, 862–889.

[163] Whitcomb JD (1992), Analysis of a laminate with a postbuckled embedded delamination, including contact effects, *J. Compos. Mater.* **26**, 1523–1535.

[164] Shivakumar KN and Whitcomb JD(1985), Buckling of a sublaminate in a quasi-isotropic laminate, *J. Compos. Mater.* **19**, 2–18.

[165] Gaudenzi P, Perugini P, and Riccio A(2001), Post-buckling behavior of composite panels in the presence of unstable delaminations, *Compos. Struct.* **51**(2), 301–309.

[166] Tay TE, Shen F, Lee KH, Scaglione A, and Sciuva MD(1999), Mesh design in finite element analysis of post-buckled delamination in composite laminates, *Compos. Struct.* **47**(1–4), 603–611.

[167] Shen F, Lee KH, and Tay TE(2001), Modeling delamination growth in laminated composites, *Compos. Sci. Technol.* **61**(9), 1239–1251.

[168] Riccio A, Perugini P, and Scaramuzzino F(2000), Modeling compression behavior of delaminated composite panels, *Comput. Struct.* **78**, 73–81.

[169] Riccio A, Scaramuzzino F, and Perugini P(2001), Embedded delamination growth in composite panels under compressive load, *Composites, Part B* **32**(3), 209–218.

[170] Pradhan B and Chakraborty D(2000), Fracture behavior of FRP composite laminates with an embedded elliptical delamination at the interface, *J. Reinf. Plast. Compos.* **19**(13), 1004–1023.

[171] Suemasu H and Kumagai T(1998), Compressive behavior of multiply delaminated composite laminates, Part 2: Finite element analysis, *AIAA J.* **36**(7), 1286–1290.

[172] Lachaud F, Lorrain B, Michel L, and Barriol R(1998), Experimental and numerical study of delamination caused by local buckling of thermoplastic and thermoset composites, *Compos. Sci. Technol.* **58**(5), 727–733.

[173] Li J and Sen JK (2001), Analysis of frame-to-skin joint pull-off tests and prediction of the delamination failure, *Proc of the 42nd AIAA/ASME/ASCE/AHS/ASC SSDM Conf*, Seattle, WA.

[174] Li J (2000), Three-dimensional effect in the prediction of flange delamination in composite skin-Stringer pull-off specimens, *Proc of Am Society for Composites—15th Annual Technical Conference on Composite Materials*, Technomic Publishing, Lancaster, PA, 983–990.

[175] Krueger R and Minguet PJ (2002), Influence of 2D finite element modeling assumptions on debonding prediction for composite skin-stiffener specimens subjected to tension and bending, NASA/CR-2002-211452, ICASE Report No 2002-4.

[176] Krüger R, Rinderknecht S, Hänsel C, and König M (1996), Computational structural analysis and testing: An approach to understand delamination growth, *Fracture of Composites*, EA Armanios (ed), Trans Tech Publications, Switzerland, **120–121**, 181–202.

[177] Parisch H (1995), A continuum-based shell theory for non-linear applications, *Int. J. Numer. Methods Eng.* **38**, 1855–1883.

[178] Parisch H (1989), A consistent tangent stiffness matrix for three-dimensional non-linear contact analysis, *Int. J. Numer. Methods Eng.* **28**, 1803–1812.

[179] Krüger R, Hänsel C, and König M (1996), Experimental-numerical investigation of delamination buckling and growth, ISD-Report No 96/3, Institute for Statics and Dynamics of Aerospace Structures, University of Stuttgart.

Ronald Krueger *joined the National Institute of Aerospace (NIA) as a Senior Staff Scientist in January 2003. He is working in the area of damage formation in advanced composite materials, focusing on the investigation of debonding in composite skin/stringer configurations using finite element analysis and fracture mechanics. Prior to joining the NIA he worked for ICASE as a Staff Scientist in Structures and Materials from August 2000 until the end of 2002. Earlier he held a NRC post-doctoral research position at NASA Langley Research Center. He joined the researchers at NASA's Mechanics of Materials Branch in 1997 where he began his investigation of debond failure in composite skin/stringer configurations. In Germany, Ronald Krueger was a research and teaching assistant at the Institute for Statics and Dynamics of Aerospace Structures at the University of Stuttgart from 1989 until 1996. He received both his diploma and his doctorate degree in Aerospace Engineering from the University of Stuttgart in Germany in 1989 and 1996, respectively.*